NAVAL POSTGRADUATE SCHOOL

MONTEREY, CALIFORNIA

THESIS

A CARBON NANOTUBE PILLAR ARRAY IONIZER FOR MINIATURE ION THRUSTER APPLICATIONS

by

Troy C. Hicks

December 2008

Thesis Advisor:	Oscar Biblarz
Thesis Co-advisor:	Marcello Romano

Approved for public release; distribution is unlimited.

REPORT DOCUMENTATION PAGE		Form Approved OMB No. 0704-0188

1. AGENCY USE ONLY *(Leave blank)*	2. REPORT DATE December 2008	3. REPORT TYPE AND DATES COVERED Master's Thesis

4. TITLE AND SUBTITLE A Carbon Nanotube Pillar Array Ionizer for Miniature Ion Thruster Applications	5. FUNDING NUMBERS
6. AUTHOR(S) LCDR Troy C. Hicks	
7. PERFORMING ORGANIZATION NAME(S) AND ADDRESS(ES) Naval Postgraduate School Monterey, CA 93943-5000	8. PERFORMING ORGANIZATION REPORT NUMBER
9. SPONSORING /MONITORING AGENCY NAME(S) AND ADDRESS(ES) N/A	10. SPONSORING/MONITORING AGENCY REPORT NUMBER

11. SUPPLEMENTARY NOTES The views expressed in this thesis are those of the author and do not reflect the official policy or position of the Naval Postgraduate School, U.S. Navy, Department of Defense or the U.S. Government.

12a. DISTRIBUTION / AVAILABILITY STATEMENT Approved for public release; distribution is unlimited.	12b. DISTRIBUTION CODE

13. ABSTRACT (maximum 200 words)

Satellites of the 'micro' class and smaller require scalable propulsion systems that minimize mass, volume and power. With a substantial reduction in ionizer size, ion thrusters may fulfill all of these requirements. This work explores field ionization with nanotube arrays for a highly-scalable ionizer.

Fabrication and testing of carbon nanotube pillar array (CPA) ionizers is undertaken at the Nanotechnology Center, NASA Ames Research Center. The devices are built using conventional photolithography, ion beam sputtering and thermal chemical vapor deposition processes. Fabrication tribulations and solutions discovered are discussed.

Testing is performed under both ultrahigh vacuum and low-pressure static gas atmospheres, with the devices configured as field electron emitters and as field gas ionizers. Argon is used as a propellant to demonstrate its suitability as an alternative to xenon. The four test samples turn on at applied fields as low as 5.3 V/μm and produce ion current densities greater than 10 mA/cm^2. Tested as field emitters, the devices show very strong correlation with Fowler-Nordheim theory and exhibit field enhancement factors as high as 1500. A qualitative analysis is made of pre- and post-test CPA characterizations.

14. SUBJECT TERMS Space propulsion; Miniature ion thruster; Small satellite thruster; Microsatellite; Nanosatellite; Picosatellite; Small Satellite; Carbon Nanotube Pillar Array; CNT ionizer; CPA ionizer;	15. NUMBER OF PAGES 113
	16. PRICE CODE

17. SECURITY CLASSIFICATION OF REPORT	18. SECURITY CLASSIFICATION OF THIS PAGE	19. SECURITY CLASSIFICATION OF ABSTRACT	20. LIMITATION OF ABSTRACT
Unclassified	Unclassified	Unclassified	UU

NSN 7540-01-280-5500

Standard Form 298 (Rev. 8-98)
Prescribed by ANSI Std. Z39.18

THIS PAGE INTENTIONALLY LEFT BLANK

Approved for public release; distribution is unlimited.

A CARBON NANOTUBE PILLAR ARRAY IONIZER FOR MINIATURE ION ENGINE APPLICATIONS

Troy C. Hicks
Lieutenant Commander, United States Navy
Bachelor of Mechanical Engineering, Georgia Institute of Technology, 1995

Submitted in partial fulfillment of the
requirements for the degree of

MASTER OF SCIENCE IN ASTRONAUTICAL ENGINEERING

from the

NAVAL POSTGRADUATE SCHOOL
December 2008

Author: Troy C. Hicks

Approved by: Oscar Biblarz
Thesis Advisor

Marcello Romano
Co-Advisor

Knox T. Millsaps
Chairman, Department of Mechanical and Astronautical Engineering

THIS PAGE INTENTIONALLY LEFT BLANK

ABSTRACT

Satellites of the ‘micro’ class and smaller require scalable propulsion systems that minimize mass, volume and power. With a substantial reduction in ionizer size, ion thrusters may fulfill all of these requirements. This work explores field ionization with nanotube arrays for a highly-scalable ionizer.

Fabrication and testing of carbon nanotube pillar array (CPA) ionizers is undertaken at the Nanotechnology Center, NASA Ames Research Center. The devices are built using conventional photolithography, ion beam sputtering and thermal chemical vapor deposition processes. Fabrication tribulations and solutions discovered are discussed.

Testing is performed under both ultrahigh vacuum and low-pressure static gas atmospheres, with the devices configured as field electron emitters and as field gas ionizers. Argon is used as a propellant to demonstrate its suitability as an alternative to xenon. The four test samples turn on at applied fields as low as 5.3V/μm and produce ion current densities greater than 10 mA/cm^2. Tested as field emitters, the devices show very strong correlation with Fowler-Nordheim theory and exhibit field enhancement factors as high as 1500. A qualitative analysis is made of pre- and post-test CPA characterizations.

THIS PAGE INTENTIONALLY LEFT BLANK

TABLE OF CONTENTS

LIST OF FIGURES

LIST OF TABLES

ACKNOWLEDGMENTS

I would like first to acknowledge the members of the NASA Ames Research Center team, without whose willingness to collaborate with me, this project would never have gotten off the launch pad. Dr. Minoru Freund for sharing my vision of where this research might lead; Dr. Cattien V. Nguyen for opening his laboratories to me, giving me full access to the facilities, equipment and materials necessary to conduct my research; Dr. Michael Oye, Brian Ribaya, Jeremy Silan, Setha Yim, Kevin Schwanfelder, and Sunny Nguyen for rendering assistance to 'the new guy' whenever I needed it.

My deep appreciation goes to Dr. Darrell L. Niemann for his invaluable teachings and tireless mentoring as I conducted this research. Being so far removed from anything I had ever undertaken before, I would never have met with such success had it not been for Darrell's insight, expertise and wisdom.

From the Naval Postgraduate School, I would like to thank Professors Oscar Biblarz and Marcello Romano for their guidance, support and for letting me take the baton and run with it. I also greatly value the trust they showed by letting me do the bulk of my work and testing at ARC away from their direct supervision. I must also thank the Space Systems Academic Group for their kind agreement to fund my weekly travel to ARC. Lastly, thank you to Dr. Jim Newman for arranging my initial meeting with the ARC team, which planted the seed for the partnership that followed.

Finally, I would like to thank most of all my family: Janis, Buzz, Clay & Amelia for their support, understanding and tolerance of all my time away, grumpy moods and general thesisitis these past six months.

THIS PAGE INTENTIONALLY LEFT BLANK

I. INTRODUCTION

A. ION ENGINE[1] HISTORY

The earliest recorded ideas for electric propulsion are notes jotted down by the renowned rocket pioneer Dr. Robert Goddard in 1906, wherein he postulated that electrostatically accelerated particles could achieve very high exhaust velocities at reasonable chamber temperatures. Between 1916 and 1917, he and his students conducted experiments demonstrating the concept by ionizing air at atmospheric pressure. However, even at this early stage, Goddard knew the ultimate application of electric propulsion would be long-duration flight in the vacuum of space [1] - [3].

The onset of World War I brought a halt to studies of electric propulsion, as scientists concentrated on chemical propulsion for weaponry, but electric propulsion was returned to the forefront of creative thought by the publication of Hermann Oberth's *Ways to Spaceflight* in 1929. Oberth realized that, with payload mass fractions typically less than 10%, chemical propulsion systems were ill-suited to long-duration spaceflight. Electrically propelled vehicles, on the other hand, could realize payload mass fractions of 50% or greater. Assuming the mission allowed for very long thrusting times, the low thrust and high specific impulse (I_{sp}) of an electric propulsion system would realize enormous reductions in propellant mass compared to chemical propulsion for the same change in velocity (ΔV) [1] - [4].

The end of World War II saw hundreds of German scientists immigrate to the United States as part of Operation Paperclip. Two of these men, Werner von Braun and Ernst Stuhlinger, were sent to Fort Bliss, Texas to research and develop rocket technology for the Army. In 1947, von Braun approached Stuhlinger and asked him to study Oberth's ideas on electric propulsion. During

[1] A note on terminology: "engine" will be used to denote the propulsion system in whole, of which the "thruster" is a subsystem.

the ensuing 10 years, Stuhlinger and his team made great strides in the study of electric propulsion, including proposals for system design as well as specific problem areas such as ion sources, beam neutralization and lightweight power supplies [1], [4].

In 1961, an ion thruster produced by the Hughes Corporation was demonstrated in a vacuum chamber simulating the space environment in which the engine would be expected to operate. Just two months later, however, NASA refocused its propulsion efforts on chemical propulsion for manned spaceflight, and its top researchers, including Stuhlinger, were reassigned to that field. Not until the 1990's did NASA revisit electric propulsion as part of its NASA Solar Electric Power Technology Applications Readiness (NSTAR) project. This project produced the 30 cm xenon ion propulsion system (XIPS) used on Deep Space 1 (DS1), a spacecraft developed specifically to investigate technologies to reduce cost and risk in future space missions. This engine, with an I_{sp} of 3100 s, accelerated the spacecraft to more than 56,000 km/h and operated for 678 total days, a record for an ion engine [1], [5], [6].

The latest development in electric propulsion is the launch of the Dawn spacecraft in September 2007 on a mission to explore the asteroids Vesta and Ceres. Dawn has three DS1 heritage XIPS, but only a single thruster is fired at any time; the other two being redundant back-ups. Dawn will be the first spacecraft ever to orbit a celestial body, study it, then depart to orbit and study a second body. It will require only 385 kg of xenon to get to Ceres, but will take eight years to arrive. Because available thrust is low, Dawn is not using a Hohmann transfer but is instead spiraling its way to the asteroid belt as depicted in Figure 1. Dawn's XIPS will provide a ΔV of more than 10,000 m/s over the lifetime of the spacecraft, far more than any other propulsion system in history. It will require, however, an accumulated thrust time of more than six years to accomplish this. Despite taking longer to reach its targets than if it were using chemical propulsion, Dawn's mission is only feasible because of its electric

propulsion system. The propellant mass required to perform the same mission with chemical propulsion would be prohibitively expensive [7].

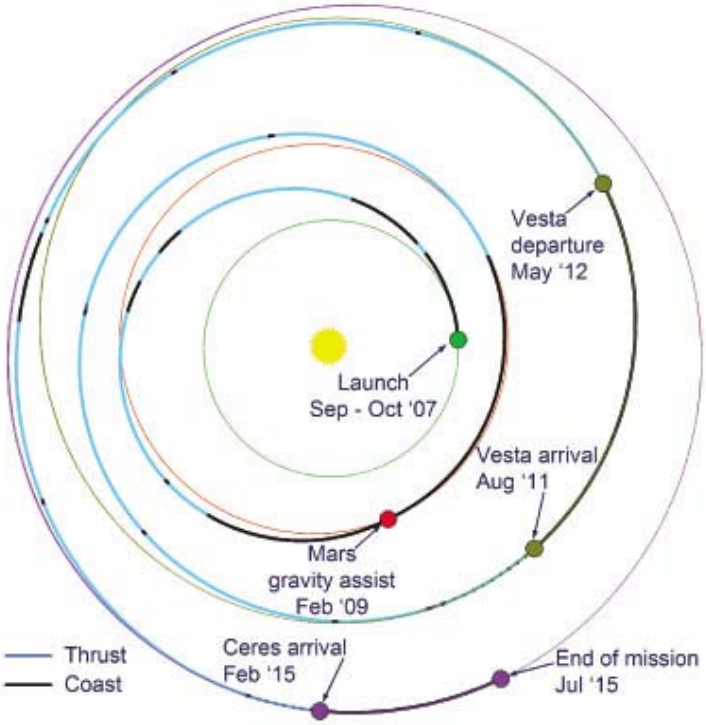

Figure 1. Dawn Mission Profile (From [7]).

B. ION ENGINE OPERATION

All ion engines comprise the same basic components, namely the power source, power processor, propellant storage and feed system, and the ion thruster, as depicted in Figure 2. The thruster subsystem includes the neutralizer, accelerator and ion source, of which there are two main classes: surface contact and electron bombardment [3].

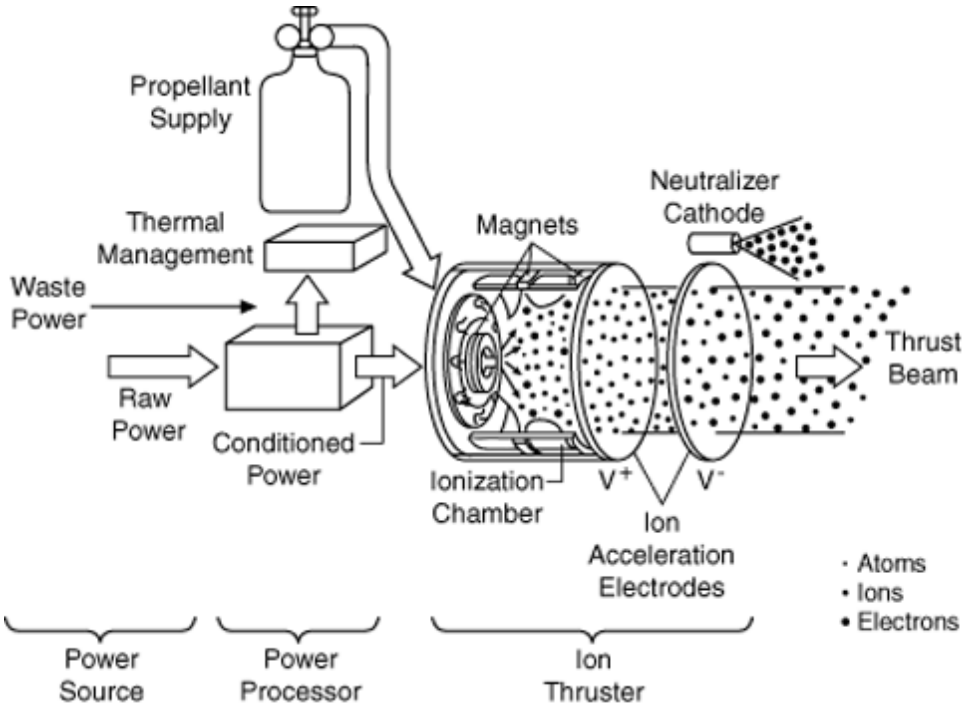

Figure 2. Ion Engine Schematic (From [7]).

Surface contact thrusters were the first type developed, with cesium being the propellant of choice. The ionizer is constructed of a refractory metal, typically tungsten, pressed and sintered into a porous matrix. In this type of thruster, the cesium vapor is back-fed to the ionizer where it flows through the matrix and is evaporated as ions from the frontal surface of the ionizer, as shown in Figure 3. Because the ionizer is back-fed, the accelerator electrode can be placed very close to the ionizer, rendering the volume of the ionization chamber very small. There is, however, a relatively large manifold behind the ionizer in which the cesium vapor is electrically heated to raise its energy level prior to entering the ionizer. The surface contact ionizer has been abandoned in favor of the electron bombardment type for two reasons. First, cesium is highly toxic and therefore undesirable as a propellant, especially in the commercial sector. Second, foreign atoms easily poison the metal matrix ionizer, which drastically lowers its efficiency [3].

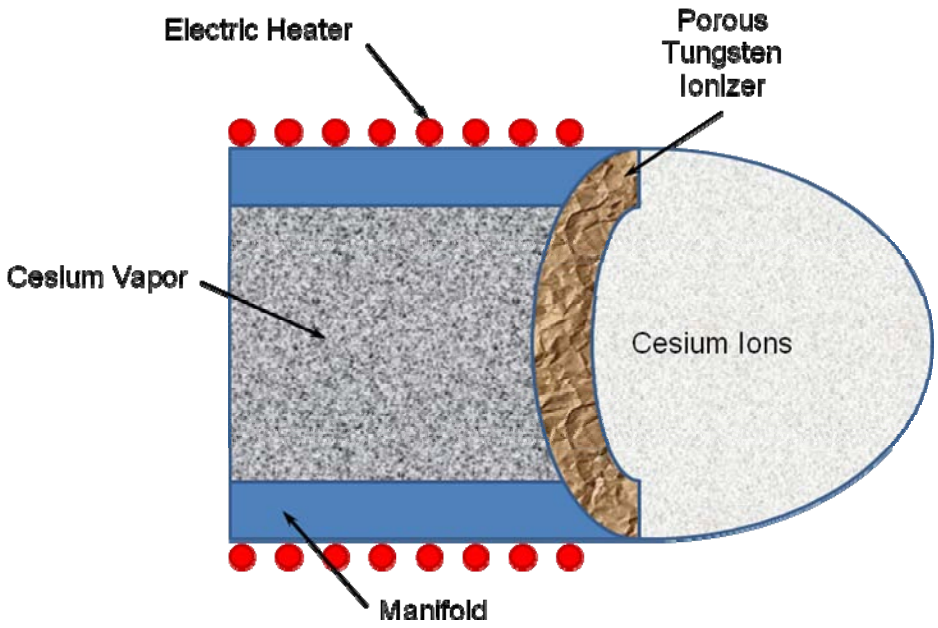

Figure 3. Surface Contact Ionizer (After [3]).

Electron bombardment thrusters use a large, cylindrical ionization chamber into which the propellant is injected from either the sides or, more commonly, the forward end. Electrons emitted by a hollow cathode into the ionization chamber are attracted to the chamber walls, which are maintained at a positive potential to the end plates. Because of this potential, the electrons are injected through a plasma sheath into a region where potential varies with both radial and longitudinal distance from the cathode. Strong magnets around the periphery of the ionization chamber set up a magnetic field that is perpendicular to the electric field, causing the electrons to oscillate and spiral their way from the cathode emitter to the anode chamber wall. It is during this trip that they collide with atoms of propellant, ionizing them, as depicted in Figure 4. The number of ions created per second per unit volume is given by

$$\frac{dn_i}{dt} = n_e n_o v_e Q_i(v_e) f(v_e) dv_e \tag{1}$$

where n_e is the electron density, v_e is the electron velocity, n_o is the atom volume density, $Q_i(v_e)$ is the cross-section for ionization function and $f(v_e)$ is the velocity distribution function. From this equation, it can be clearly seen that the most desirable performance is achieved by generating electrons with the highest possible velocity and the longest possible life span [3], [8].

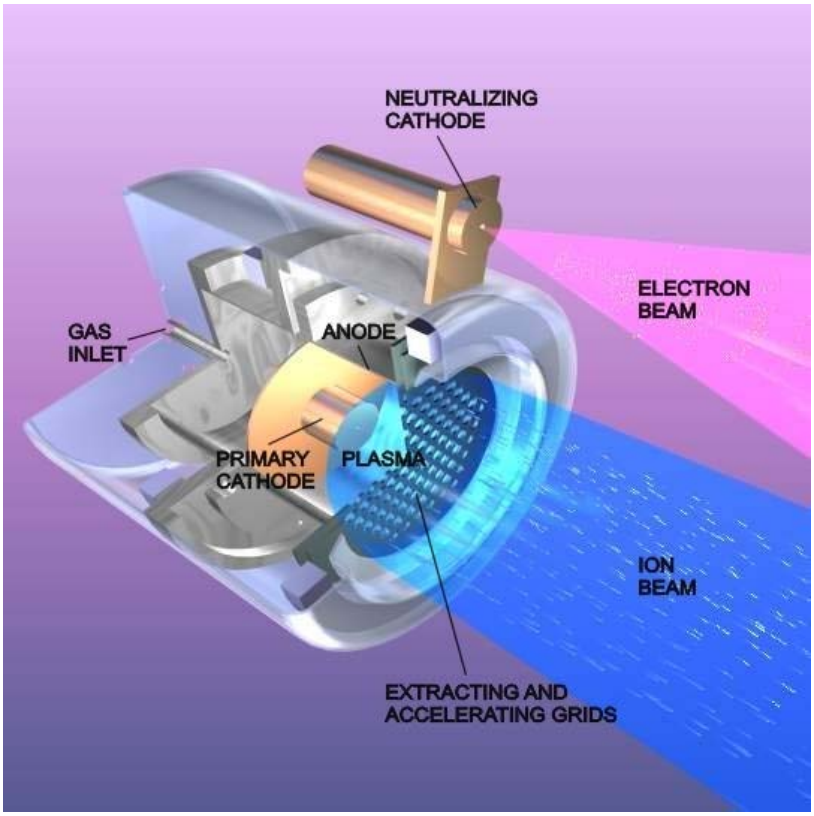

Figure 4. Electron Bombardment Thruster (After [2]).

Regardless of the ion source, all ion thrusters use an arrangement of electrodes to accelerate the ions and create the collimated ion beam which propels the spacecraft. The exhaust velocity of the ion beam is given by

$$v = \sqrt{2\frac{\varepsilon}{\mu}V_{acc}} \tag{2}$$

where V_{acc} is the voltage difference across the grids, ε is the charge of the ions, and μ is their mass. Very high exhaust velocities, typically in the range of 30 to 200 km/s, are thus achieved without excessive chamber heating [4].

Some early ion thrusters used linearly slotted electrodes, but all modern designs use a gridded electrode containing hundreds or thousands of small apertures. This electrode comprises two parallel grids with concentric apertures. The first grid is charged highly positive, the second highly negative. This arrangement causes the ions being created in the ionization chamber to be attracted to the accelerator grid, focused by the optical design of the grid, and then discharged from the thruster. The total thrust generated by an ion thruster is given by

$$F = \dot{m}v \tag{3}$$

where $\dot{m}$ is the propellant mass flow rate and v is the exhaust velocity. The current across the accelerator is given by

$$I = \dot{m}\left(\frac{\varepsilon}{\mu}\right) \tag{4}$$

which assumes an ideal thruster and a supply of 100% singly ionized particles. Rearranging equation (4) then substituting it and equation (2) into equation (3) gives the expression for total thrust in terms of parameters of interest to this discussion:

$$F = I\sqrt{2\frac{\mu}{\varepsilon}V_{acc}}. \tag{5}$$

As can be seen from equation (5), for given current and voltage parameters, the thrust is proportional to the mass-charge ratio [4], [8], [9].

Because the ion thruster is expelling positive ions, it will cause a build-up of negative charge on the spacecraft if nothing is done to counteract this effect. Spacecraft charging is undesirable because it results in attraction of the exhausted particles back to the spacecraft, which can cause a number of adverse effects, including shorting out of electrical connections, interference with instruments and coating of optics. Furthermore, a sufficiently intense field build-up around the spacecraft will impede, and eventually stop, the very flow of ions on which the propulsion system is reliant. To prevent this charging effect, electrons collected by the anode of the ionization chamber are routed to the neutralizer subsystem, a second cathode at the thruster discharge. Here the electrons are injected into the exhaust beam, neutralizing it, as depicted in Figure 4 [4], [8], [9].

C. APPROACH

The overarching advantage of ion propulsion is the reduction in propellant mass that results in an increase in payload mass-fraction of up to ten-fold when compared to chemical propulsion. Because the thrust is typically less than 0.5 N, long thrusting times are required. Therefore, the mission profiles for ion propulsion include station-keeping, drag compensation, orbit adjustment, orbit transfer and interplanetary flight. Of these, all but the last are applicable to satellites of the 'micro' and 'nano' classes[2] that are receiving increased attention in the modern era as program managers seek technologies to reduce risk and cost. There are, however, two major roadblocks to the adaptation of existing ion thrusters to small sats: scalability and cost. The use of strong magnets and their associated volume and mass constraints are the first problem. Furthermore, the power levels required by these thrusters, which range from many hundreds to a few thousands of watts, simply cannot be supplied by the solar arrays of small

[2] Hereafter referred to collectively as "small sats."

sats. Therefore, both physical packaging and power requirements preclude scaling current ion thruster technology to a size suitable for this new class of spacecraft.

The highest efficiency for ion propellants is achieved with mercury, cesium or xenon because of their high mass-charge ratio, but for I_{sp} greater than approximately 6,000 s, the efficiency of these propellants is essentially equaled by that of argon. Because cesium and mercury are generally undesirable as propellants due to their toxicity, and because the cost of xenon, the currently favored propellant, is extremely high, there is an interest in using argon as a propellant. The advantages of argon go beyond its low cost to include its inertness, which makes it safe to handle and nonreactive with spacecraft components, its lower ion kinetic energy, which increases electrode life, and its low ratio of doubly to singly ionized ions, which increases accelerator performance [10].

This thesis explores a revolutionary concept for the miniaturization of the ionization chamber in an ion thruster: the use of a carbon nanotube pillar array (CPA) as a gas ionizer. Such an ionizer will enable the ion thruster to be scaled to sizes suitable for small sats. These CPAs exhibit an extremely high field enhancement factor (γ) that should result in ionization at power input levels orders of magnitude lower than what is currently required for electric propulsion. At the same time, the experiments conducted to support this thesis use argon as a propellant, demonstrating its suitability as a low-cost, efficient alternative to xenon. Because the argon can be cold-fed to the ionizer, this design is essentially a surface contact ionizer without the heating manifold required by legacy thrusters of that type. This shrinks the ionization chamber to less than 1% of the volume of a comparable electron bombardment ionizer, while allowing it to operate on less than 1% of the power required for that thruster. Finally, the high γ means increased ionizer efficiency.

Chapter II reviews theories of field emission and field ionization, basics of CPA geometry, and previous studies of CPAs as gas analyzers. Chapter III discusses the design and fabrication of the CPAs used in this research as well as the experimental apparatus and associated equipment used to analyze them. Chapter IV gives the summary of experimental results and Chapter V contains a summary, conclusions and recommendations for future research in this area.

II. BACKGROUND OF CARBON NANOTUBE PILLAR ARRAY FIELD EMISSION STUDIES

A. FIELD EMISSION / FIELD IONIZATION

Field emission is the emission of electrons from the surface of a condensed phase, usually a metal, under the motivation of an intense electric field, typically 3-6 kV/μm. Field emission involves the tunneling of electrons with energies below the Fermi level through the potential barrier at the emission interface, as opposed to other types of electron emission, such as thermionic or photoemission, in which only those electrons with energies above the Fermi level escape over the potential barrier [11].

Field ionization is essentially the opposite of field emission. In field ionization, an energized tip ionizes atoms of gas, usually called the analyte. This moniker is used extensively in the literature because field ionization is most commonly used to ionize gas for the purposes of analysis such as mass spectrometry or simple detection/warning. This thesis will usually refer to the gas being ionized as the propellant, since that is the subject of interest. The field ionization tip (FIT) is sometimes referred to as an emitter, however this is incorrect. In fact, the tip is an absorber. As the electric field ionizes the propellant, electrons tunnel from the atoms being ionized into the tip. The electric field strength required for field ionization is considerably higher than that required for field emission, approximately 20-50 kV/μm. The probability of ionization for a given atom is dependent on its charge, the ionization potential and the applied field [11].

The ion current supplied by a field ionization tip is limited by two extremes. At sufficiently high field values, all particles approaching the ionizer become ionized prior to arriving at the tip. Therefore, the ion current is limited by the supply of propellant. At field values such that the ionization rate is very small

compared to the supply rate, the ionization current is limited by the lifetime of the ions, which is a function of their momentum, mass and radius [11].

B. CARBON NANOTUBES AND PILLAR ARRAYS

Carbon nanotubes (CNTs) are cylindrical molecules of pure carbon whose atoms are arranged in a graphitic structure. They can be formed either as single-walled structures (SWCNTs), as shown in Figure 5, or as multi-walled structures (MWCNTs), as shown in Figure 6. The structure in Figure 6 is known as a Russian Doll MWCNT due to its structure of concentric individual CNTs. There is another type of MWCNT known as the Parchment model, wherein the entire CNT is a continuous graphitic sheet curled upon itself like a roll of parchment.

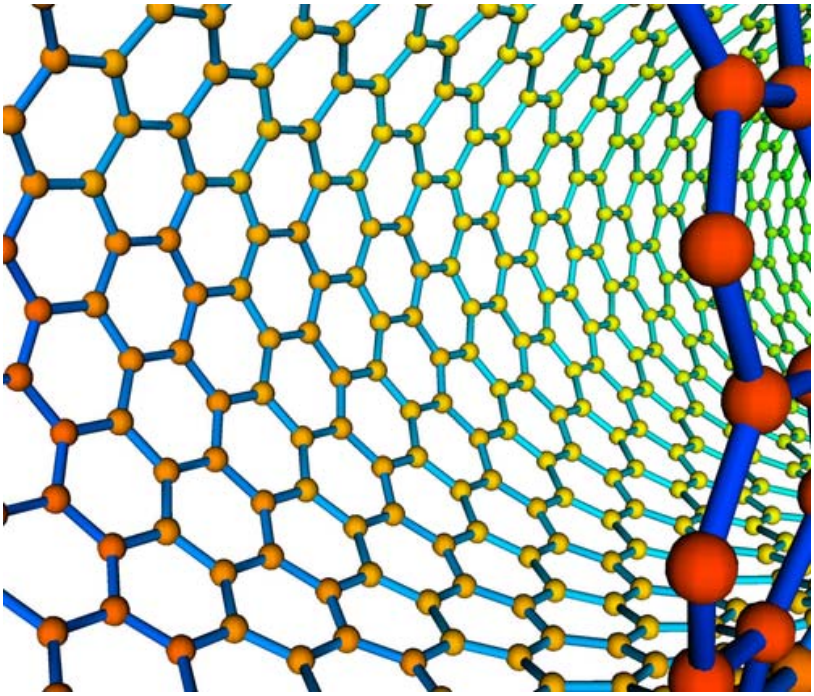

Figure 5. Single-Walled CNT (From [12]).

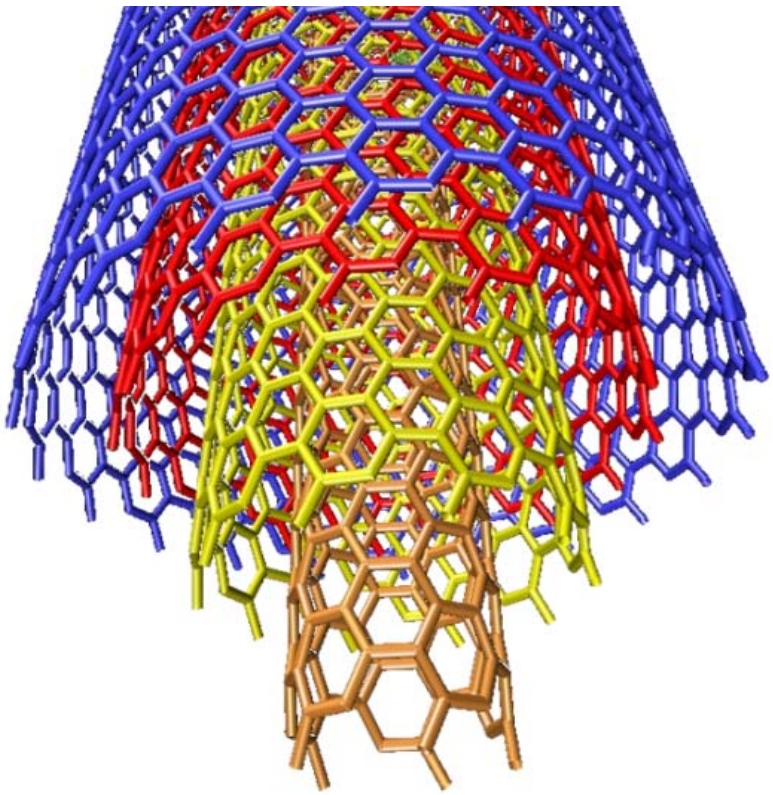

Figure 6. Multi-walled CNT (From [13]).

Because the carbon-carbon bond is extremely strong, CNTs possess a host of highly interesting properties. They are the strongest and stiffest material known to man. Their tensile strength of 150 GPa is approximately 200 times that of steel; their Young's modulus of 1 TPa makes them five times stiffer than steel, but at only one-quarter the density. They are highly thermally conductive, with a conductivity 15 times that of copper, and they remain stable at temperatures approaching 3000ºC in vacuum. Of most interest to this research is their electrical conductivity, which enables them to carry a current density more than 1000 times higher than silver [14].

A CNT pillar array (CPA) electrode is an electrode composed of a patterned array of pillars. Pillars are defined as localized, vertically oriented, well-ordered groups of CNTs. The vertical orientation and order result from van der Waals forces during the growth of high density CNTs; it is not evident in medium and low-density growth. Low-density non-aligned growth is shown in

Figure 7. In this particular experiment, the undesirable growth resulted from a concentration of carbon-bearing gas too low for the growth conditions. Compare this to the much more dense growth seen in Figure 8 and Figure 9. The γ of the pillars is dependent on geometric factors such as pillar diameter, height, spacing, and uniformity; CNT diameter and uniformity; and the degree to which the CNTs are oriented parallel to one another.

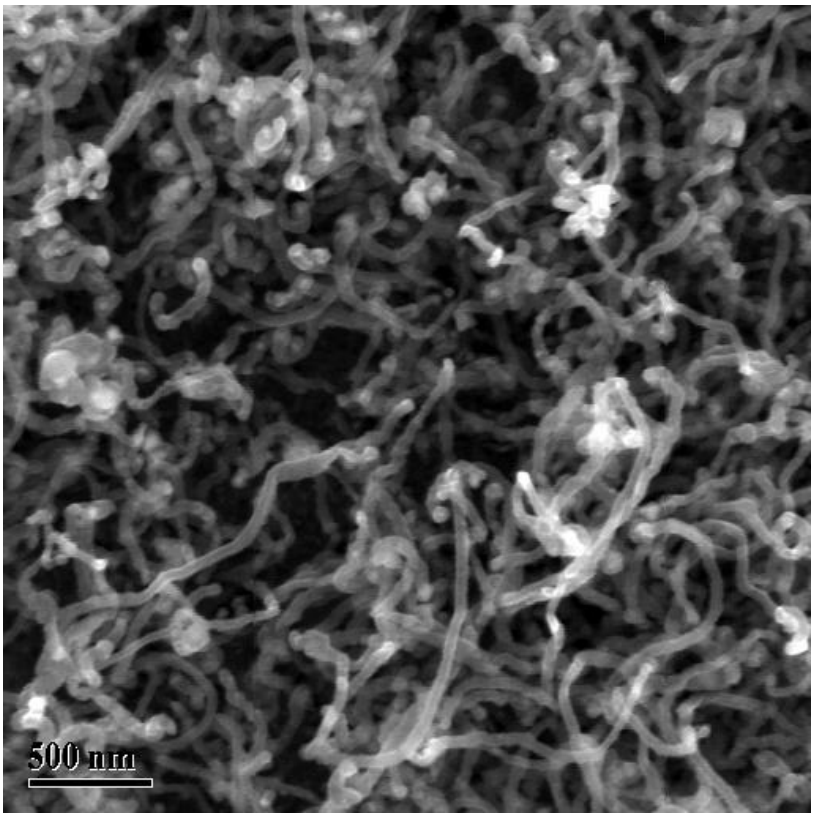

Figure 7. Low-density Non-aligned CNT Growth.

The preferred method for creating CPA electrodes is thermal chemical vapor deposition on a catalytic substrate patterned by conventional photolithography. More detail on fabrication of CPA electrodes is given in Chapter III. Experiments on CPA electrodes have shown them to be preferable to both single CNTs and CNT film arrays (CFAs). CFAs are similar to CPAs, but are very short compared to their width, i.e., they are low aspect ratio structures.

The very low aspect ratios of CFAs result in much smaller γ values than those exhibited by high aspect ratio structures such as CPAs and single CNTs. Single CNTs produce some of the highest observed γ of any structure, due mainly to their extreme sharpness, having tips mere nanometers across. This implies that sparsely arranged single CNTs would be preferable to any sort of film or pillar array; however, CPAs have three distinct advantages over single CNTs. First, the mutually supporting structure of a CPA results in increased robustness compared to stand-alone CNTs. Second, due to limitations in the control of the fabrication process, pillars exhibit a noticeable increase in height uniformity. This is directly related to two key attributes of the device: performance and longevity. Lastly, because the van der Waals interaction is only present in dense growth, pillars are aligned much more perpendicularly to the substrate than single CNTs [15]. This can be clearly seen by comparing the high density, well-aligned growth shown in Figure 8 and Figure 9 to that shown in Figure 10, where the CNTs are individually wavier and at the same time less aligned with each other.

The main drawback to CPAs is that the CNTs on the interior of the pillars contribute relatively little to the field enhancement of the array, but this disadvantage is outweighed by the fact that pillars are much more resistant to CNT burnout. Arrays of single CNTs can suffer hotspots due to irregularities in the individual characteristics of the CNTs, which can in turn result in large areas of the array burning out, seriously degrading electrode performance. In a CPA this is unlikely because the pillars act in accordance with the average characteristics of their constituent CNTs. Because pillars comprise so many CNTs, this average tends to be consistent across the array, producing uniform electric field characteristics and preventing formation of hotspots. Some CNTs in CPAs will burn out during the electrode conditioning phase, but a conditioned CPA electrode will exhibit very consistent and reproducible performance characteristics.

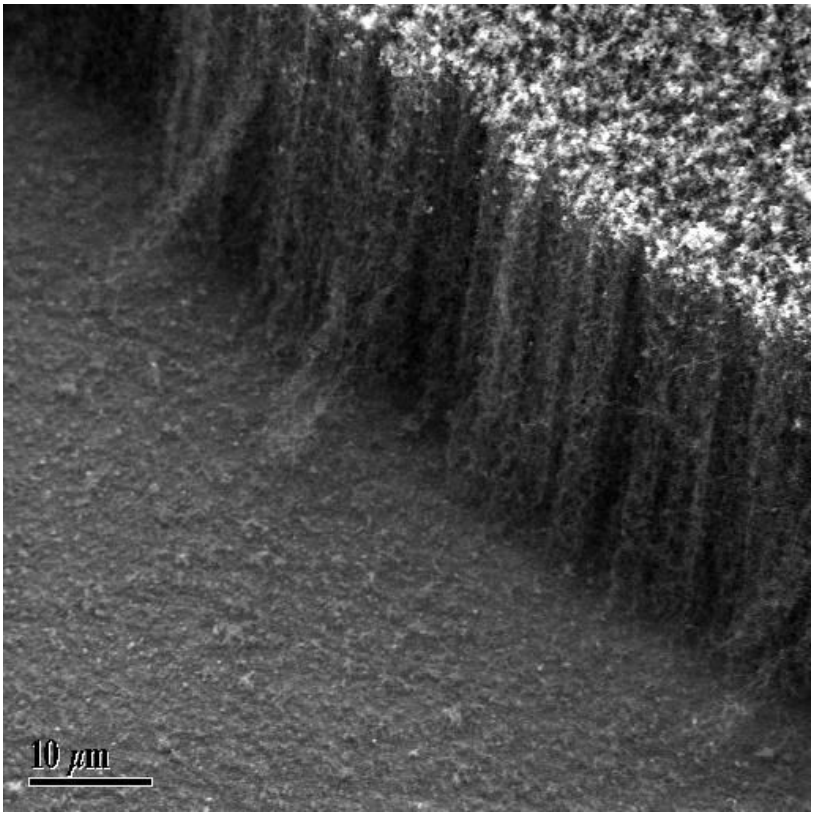

Figure 8. CNT Growth on Fe/Si Substrate.

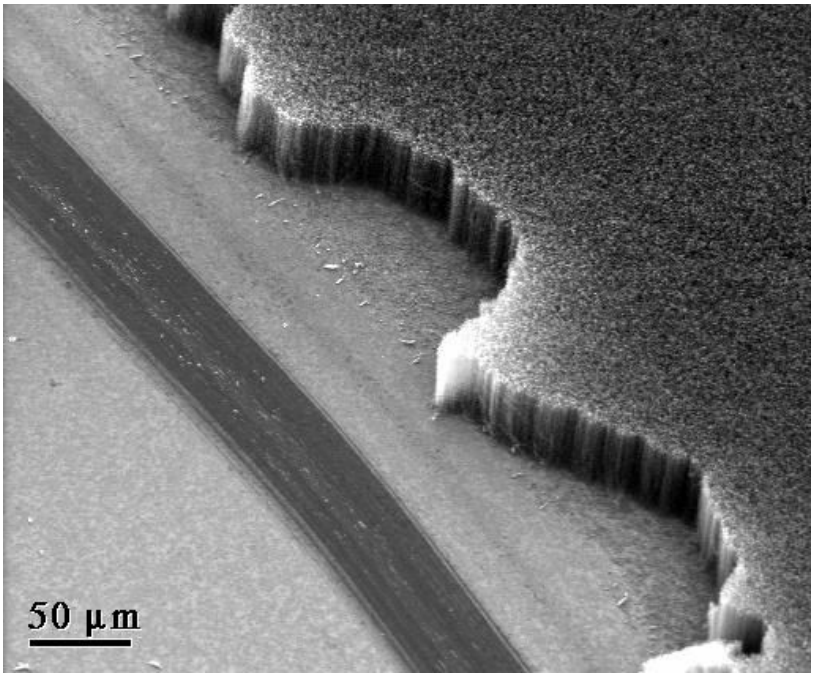

Figure 9. CNT Growth on Fe/Si Substrate.

C. PREVIOUS STUDIES

The idea of using nanotechnology to produce small field ionizers has emerged relatively recently. In 2004, a team from Rennselaer Polytechnic Institute (RPI) explored the use of tungsten nanorods as gas ionizers for the purposes of creating a battery-powered gas chromatograph. In their study, the researchers found that ionization of gaseous argon was possible with anode voltages as low as three volts, and that ion currents of tens of microamperes were generated. They also showed that the field ionization process did not significantly alter the nanorods. By contrast, the silver cathode was significantly degraded, evidenced by the formation of bubbles in the silver due to argon's insolubility in the metal. The density of bubbles was approximately ten times that of the nanorods, indicating that cathode replacement may be required with some frequency in these devices. These devices are also less robust than CPAs due both to the single nanorod structure as well as the extremely tight tolerance on the electrode gap spacing, which was only about 0.4 μm [16], [17].

Other studies have also considered carbon nanotube ionizers for similar gas analysis applications. These studies found that, while breakdown voltages are higher for carbon nanotubes than for tungsten nanorods, the ionization currents are also much higher. For example, the breakdown voltage for argon was found to be approximately 240 V, but the ionization current is between 320 and 460 μA, depending on gas concentration. Also, ionization current was found to increase with gas concentration, while the breakdown voltage remained relatively constant. This is convenient because it implies that propellant ionization currents could be quite high for a given input voltage at propellant concentrations of interest [17].

More recent research of CNT field ionizers for gas analysis was performed by a team at the Massachusetts Institute of Technology (MIT). Using plasma-enhanced chemical vapor deposition (PECVD), they grew sparsely arranged single CNTs on a porous silicon substrate. As shown in Figure 10, the analyte

flows from the back surface of the device, through the porous substrate, and then along the length of the CNTs until it encounters a sufficiently strong field to be ionized. This arrangement gives the propellant much greater access to the CNTs than flowing it across the surface of the substrate. A flow-past design encounters higher resistance to flow as well as greater field shadowing of the CNTs than does the flow-through design of the MIT ionizer.

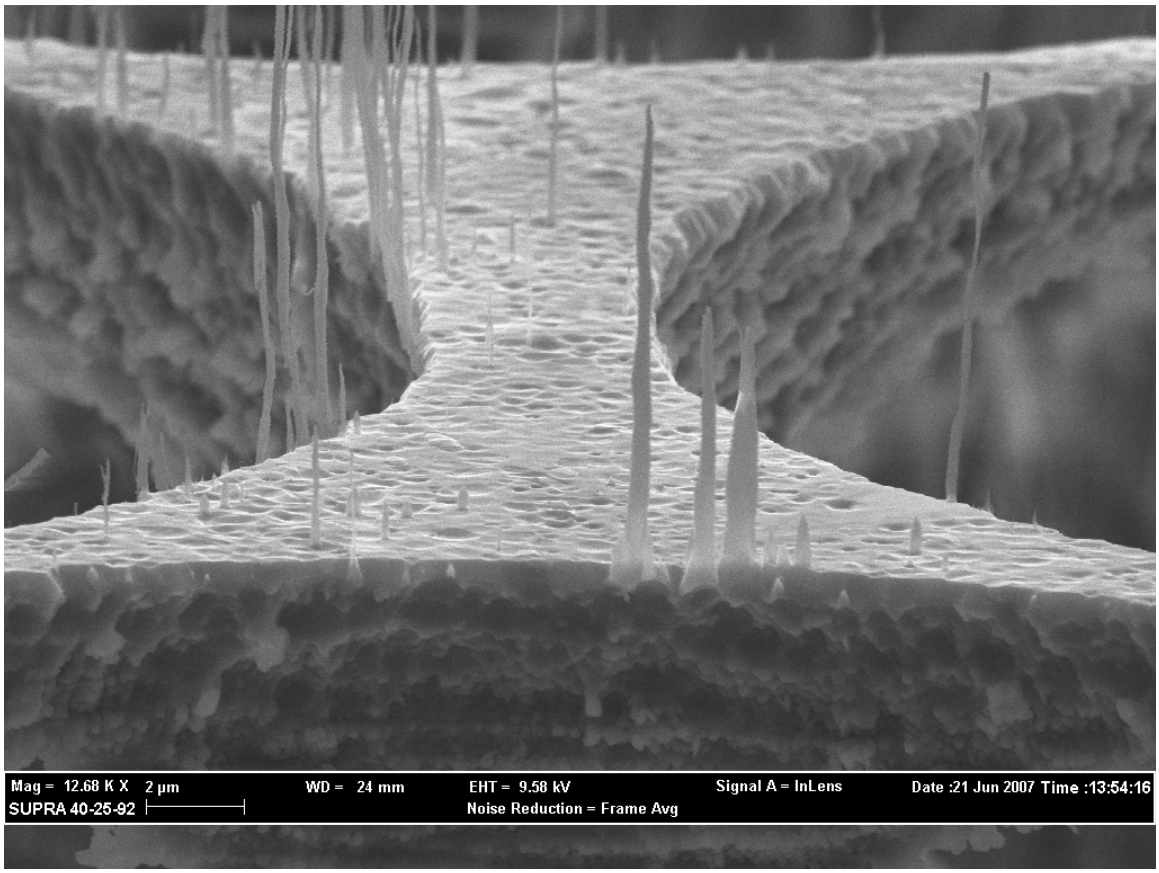

Figure 10. Sparse CNTs on Porous Silicon Substrate (From [18]).

A schematic of the MIT field ionizer is shown in Figure 11. This arrangement is very conducive to maximizing propellant access to the ionization region. The ions are extracted by the gate electrode to protect the tips, and are then focused by the ion optics for acceleration, generating thrust.

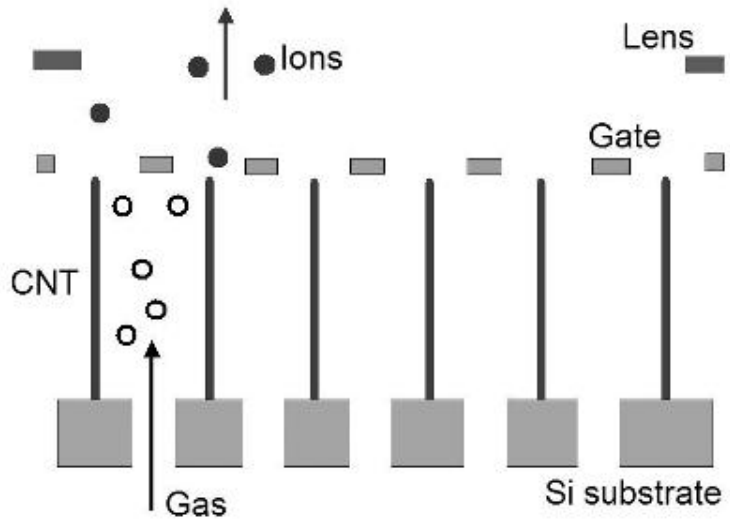

Figure 11. Schematic of a Flow-through Gas Analyzer (From [18]).

Another interesting feature of the MIT device is the gate electrode. This gate, biased negative with respect to the CNT tips, extracts the ions from the region of the CNTs, preventing back-ion bombardment. This is highly desirable because back-ion bombardment can severely erode the CNTs, considerably reducing the device's lifespan. Because these devices are envisioned integrated into ion thrusters with firing times measured in years, preservation of the ionizer tips is a high priority. Previous gate designs have resulted in unacceptable blockages of the CNTs, as shown in Figure 12. Clearly this arrangement precludes maximum access of the propellant to the ionization region in the vicinity of the tip.

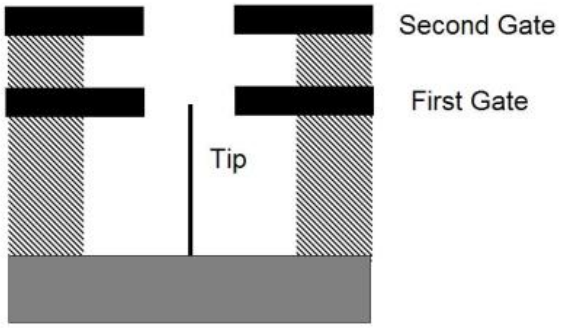

Figure 12. Gated CNT Field Ionizer (From[18]).

THIS PAGE INTENTIONALLY LEFT BLANK

III. EXPERIMENTAL APPARATUS

A. CARBON NANOTUBE PILLAR ARRAY ELECTRODE FABRICATION

All electrodes discussed in this thesis were fabricated by the author in the ARC Nanotechnology Center under the guidance of Dr. Darrell Niemann. The initial concept for the electrode was a patterned CPA grown on a perforated silicon substrate in a structure similar to that shown in Figure 11, but with pillars surrounding the through-holes, vice single CNTs, as shown in Figure 13. The process flow for fabrication of this electrode is shown in Figure 14 and Figure 15.

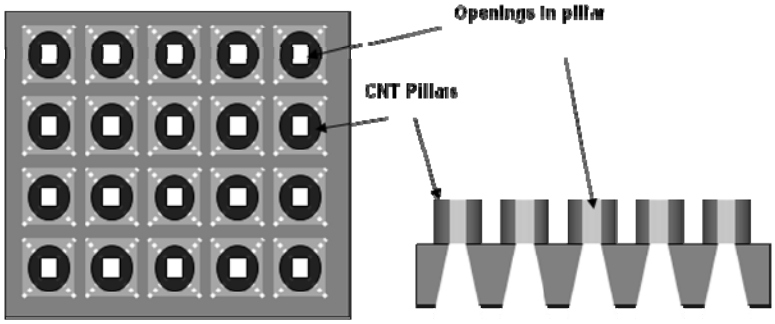

Figure 13. Original Design Concept for a Flow-Through CPA Ionizer.

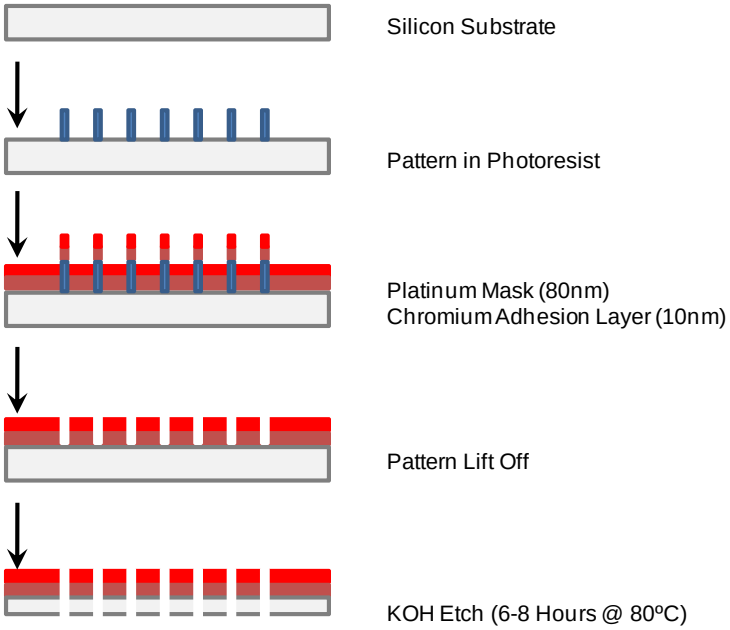

Figure 14. Process Flow Diagram for Fabricating Perforated Silicon Wafer (Wafer Thickness Not to Scale).

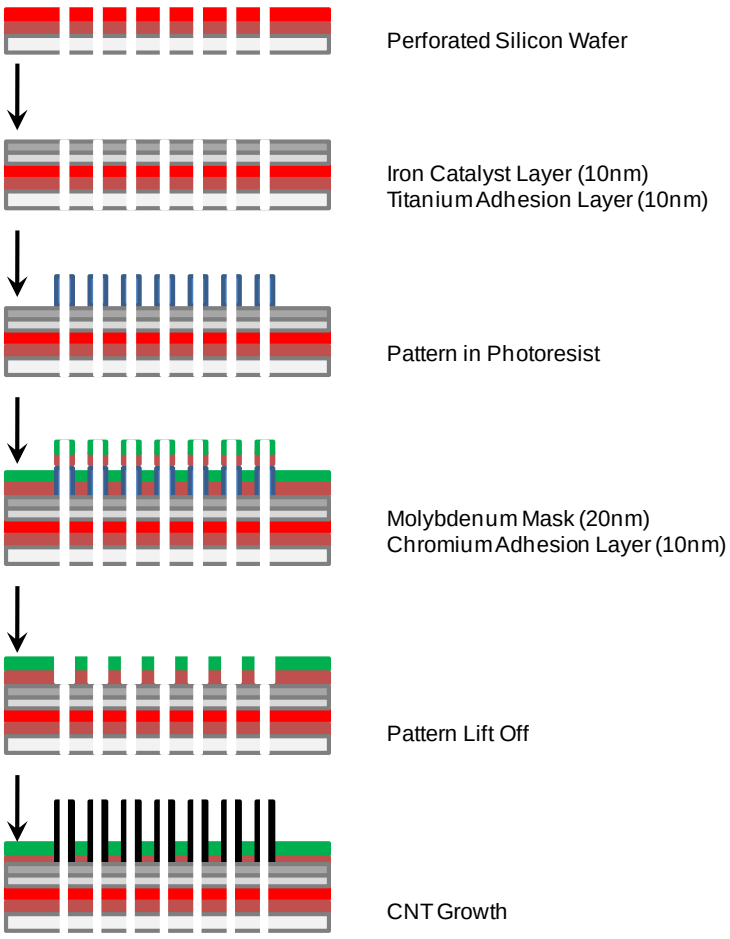

Figure 15. Process Flow Diagram for Fabricating Flow-Through Type CPA Electrode (Wafer Thickness Not to Scale).

A wet etch procedure was attempted for perforating the silicon wafer. The procedure for wet etching is described in detail in Appendix A, Section B, and is diagramed in Figure 14. Wet etching involves using a strong base, in this case potassium hydroxide (KOH), to etch through the unmasked areas of the substrate, while ideally having no effect on the masked areas. Early experiments to determine etch rate used both nickel and titanium as mask materials. Because most metals exhibit poor bonding with silicon, 10 nm of chromium (Cr) was sputtered on to act as an adhesion layer, followed by a layer of masking metal. The detailed procedure for sputtering is found in Appendix A, Section A.

Different mask thicknesses were tried, ranging from 10 to 30 nm; however, none of them survived the etching process more than two hours.

In order to determine etch rate and mask feasibility, small squares of masking tape were applied to the silicon wafer prior to sputtering the adhesion and mask layers. Following the sputtering, the tape was peeled off, revealing the bare silicon area to be etched. Figure 16 shows a nickel-masked sample that was etched for only one hour. As can be seen, significant degradation of the mask was apparent after this time. The surface should appear smooth and clear, like a mirror, with only the two squares having been etched. The sample was then examined with an optical microscope and the etch rate was estimated to be 20-25 μm per hour. Based on this observation, it was estimated that six hours would be required to completely perforate the silicon wafer, assuming that no mask was applied to the back of the sample. Not back-masking allows the wafer to be etched from both sides simultaneously. The advantage of this technique is that single masking is a simpler and less time-consuming procedure. The disadvantage is that it results in a more fragile sample.

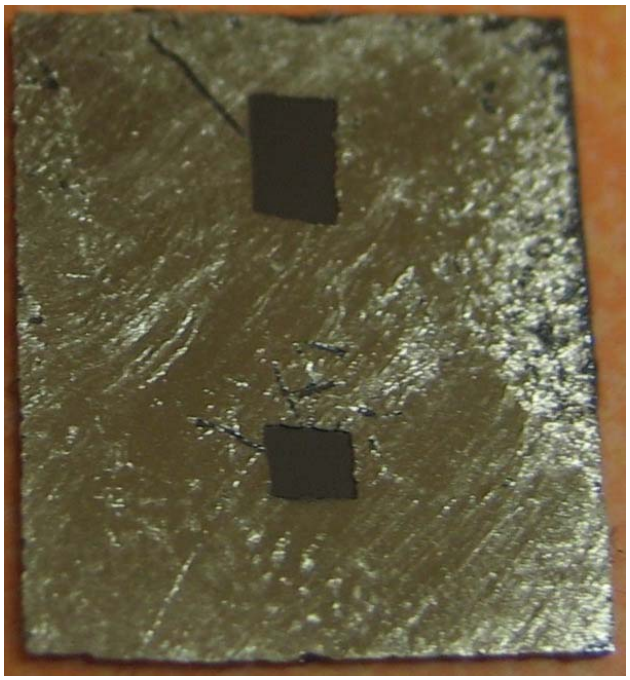

Figure 16. 10 nm Nickel-Masked Sample Etched for One Hour in 50% Potassium Hydroxide at 80ºC.

Figure 17 shows a close-up example of mask failure. Of particular note is the square shape apparent at each failure point; this is because the crystalline structure of the silicon wafers being used is 1-1-1, which means the crystal bonds are at right angles to one another. Because the KOH etches atomic bonds, not atoms themselves, it creates these characteristic square shapes wherever it is able to penetrate the mask.

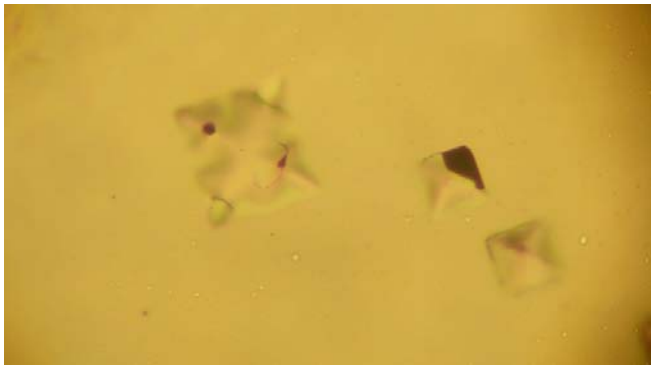

Figure 17. 10 nm Nickel Mask Failure After One Hour of Etching in 50% Potassium Hydroxide at 80ºC (50x Magnification).

Following the experiments with nickel and titanium masks, it was determined that neither would survive the time required to fully perforate the wafer. Platinum is the masking metal of choice, as it is supposed to have an etch rate of zero. However, platinum masks of 20 and 40 nm failed just as the previous masks had. The next experiment involved sputtering 40 nm of platinum, rotating the sample, then sputtering an additional 40 nm of platinum. The rotation was added to the procedure because the sputterer does not deposit a layer of uniform thickness. For this reason, it was thought that rotating the sample would enhance the uniformity of the mask and thereby preclude KOH intrusion. This mask survived until the wafer was perforated, a procedure that required six and one-half hours. The mask did not survive intact, as shown in Figure 18 and Figure 19. Note also, in Figure 18, three of the four corners of the sample are broken away due to the aforementioned increase in sample fragility.

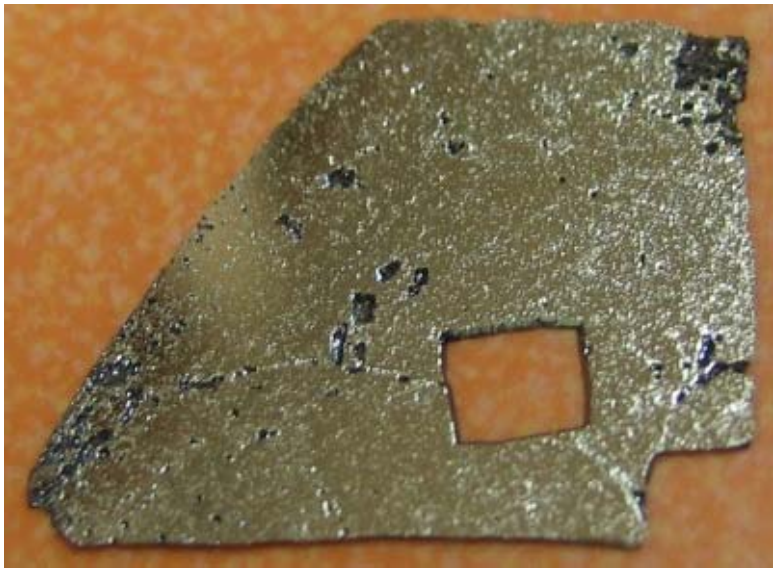

Figure 18. Close-up of 80 nm Platinum Mask After Six and One-Half Hours of Etching in 50% Potassium Hydroxide at 80ºC.

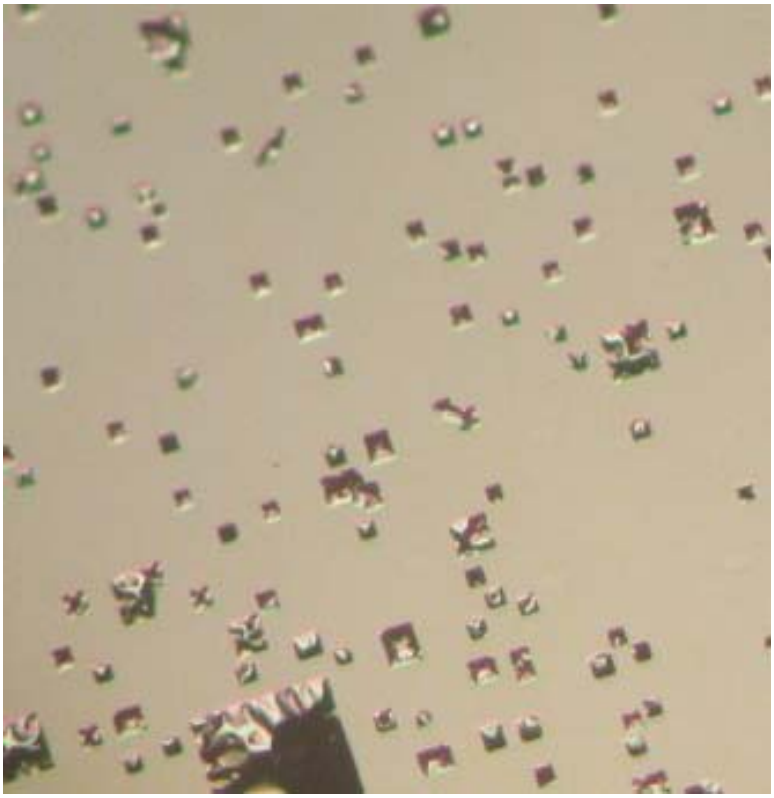

Figure 19. 80 nm Platinum Mask After Six and One-Half Hours of Etching in 50% Potassium Hydroxide at 80ºC (5x Magnification).

A second problem with this mask was that its thickness was believed to be enough to make pattern lift off difficult. In order to test this theory, a sample was fabricated using the procedure shown in Figure 14. As seen in this diagram, in order for the pattern to be lifted cleanly off, the photoresist must be thicker than the mask layer. If the mask layer is too thick, the solvent being used for lift off will be blocked from dissolving the photoresist and the pattern will be unrecoverable.

This theory was borne out by patterning a sample then masking it with 80 nm of platinum. The pattern was incompletely lifted off, despite using boiling, ultrasonic and mechanical agitation techniques. Also, areas that were not perfectly cleaned of photoresist prior to sputtering the platinum were lifted off. It was clear that a thicker mask layer, as required to withstand the etching procedure, would render the sample completely unviable. For this reason, and due to constraints of time, fabricating a flow-through electrode was abandoned in favor of experimenting with flow-past electrodes.

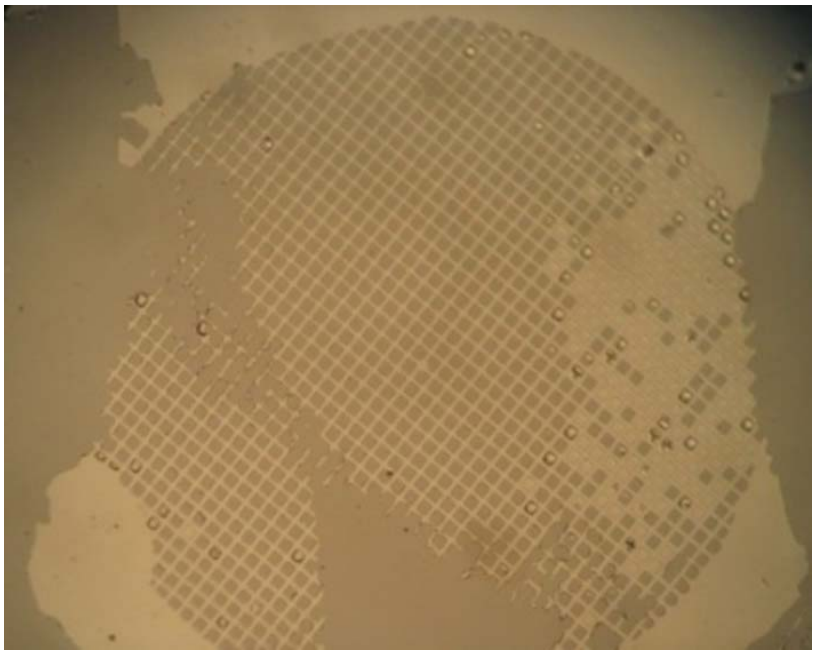

Figure 20. Pattern Damage Following Lift Off of 80 nm Platinum Mask. The Lighter Areas are Still Masked with Platinum while the Darker Areas are Bare Silicon (5x Magnification).

The fabrication process for a flow-past CPA electrode is shown in Figure 21. This process is identical to that shown in Figure 15 except it begins with an imperforated silicon wafer. Detailed procedures for each step in this process are given in Appendix A. More than 60 CPA electrodes were fabricated following this procedure, but most were not of high enough quality to warrant testing in the vacuum chamber. There were various types of deficiencies evident in these electrodes; these deficiencies and the experiments conducted to correct them, are described below.

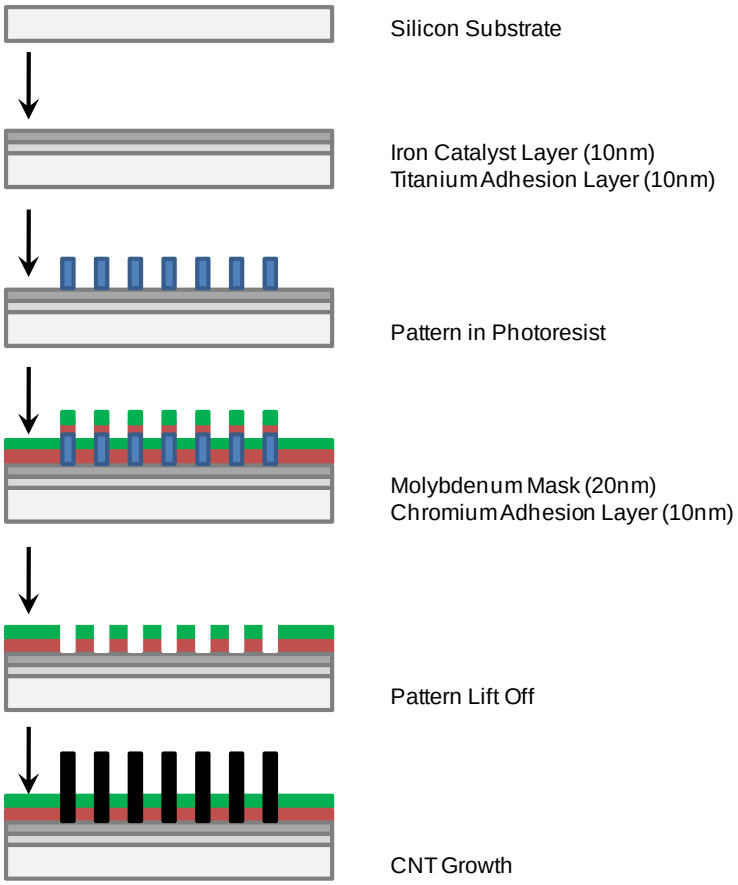

Figure 21. Process Flow Diagram for Fabricating Flow-Past Type CPA Electrode (Wafer Thickness Not to Scale).

The major problem encountered during fabrication was low-quality CNT growth. Low-quality growth is growth which is either sparse, poorly-aligned, or

both. Since CPA electrode performance is directly tied to the density and alignment of the CNTs, high-quality growth is vital. Low-quality growth can result from a variety of fabrication errors. One possibility is insufficient thickness of the catalyst layer. In previous experiments conducted at NASA, 7 nm of high purity (99.999%) iron (Fe) resulted in tall, well-aligned growth, but early examples fabricated this way for this research showed extremely sparse growth, as shown in Figure 7. To promote denser growth, the thickness of the Fe layer was increased to 10 nm. While the growth for these samples was indeed denser, it still did not exhibit the very dense, well-aligned structure shown in Figure 8 and Figure 9. All of the growth for this research was performed in the same furnace in the ARC Nanomaterials Synthesis Laboratory.

In order to determine whether other elements of the fabrication process might be responsible for the poor growth, three separate samples were made, one with Fe on Cr, one with Fe on Molybdenum (Mo) and one with just Fe. CNTs were grown on these samples via thermal chemical vapor deposition (TCVD). Detailed procedures for TCVD are given in Appendix A, Section D.

TCVD is a process by which nanotubes are grown on a substrate in a reaction vessel (RV). The RV for these experiments was a quartz glass tube, one inch in diameter and approximately 25 inches long. The RV is heated in a furnace until a steady-state growth temperature is reached. During this heating process, argon is flowed through the RV to displace contaminants such as atmospheric oxygen, which interferes with the TCVD. Upon reaching steady state, two gases are fed into the RV: a process gas, in these experiments hydrogen and a carbon-bearing gas, usually ethylene. Nanotubes grow on the metal catalyst where the carbon-bearing gas is thermally cracked at the surface. The catalyzed reaction results in the carbon forming nanostructures. If the catalyst layer is poorly adhered to the substrate, it may be lifted with the growth of the nanotubes and remain at their tips. This can be seen in Figure 8 where the Fe, which has been lifted by the growing CNTs, appears as bright spots at their tips.

The samples were placed in the RV with the Fe as the most upstream, the Fe/Cr in the middle and the Fe/Mo the most downstream. The results were that the Fe sample grew the CNTs shown in Figure 8 and Figure 9, the Fe/Cr grew CNTs similar to Figure 7 and the Fe/Mo grew barely any CNTs at all. It was suspected that the reason for the failure of the Fe/Mo sample to grow any CNTs was that, being the most downstream sample, it had been supplied with an insufficient amount of carbon. The fact that the Fe/Cr sample grew so poorly while sitting immediately adjacent to the Fe sample which grew so well led the researchers to believe that the Cr adhesion layer was interfering with the growth process. A second growth was conducted with only the Fe/Mo and Fe samples, with the Fe being placed downstream of the Fe/Mo sample. The result of this experiment was that the Fe sample again showed very good growth characteristics, while the Fe/Mo sample exhibited growth which was better than in the first experiment, but still not of adequate quality. A third growth was performed, with only a Fe/Mo sample in the furnace, and the results were much the same.

The structure of CNTs grown on Fe with no adhesion layer is not very robust. Because this electrode is envisioned as an ionizer in a thruster for space applications, its structural integrity is of interest to this research. For this reason, another trial was conducted with titanium (Ti) as the adhesion layer, and this resulted in acceptable CNT growth, though still not of the quality exhibited by the Fe samples. Following this experiment, all subsequent electrodes were fabricated using 10 nm of Ti for adhesion of the catalyst layer to the substrate. The catalyst thickness was likewise fixed at 10 nm.

Another issue with the growth process was the mask layer of Mo/Cr consistently breaking down. Looking at Figure 22, it can be seen that CNTs have grown on the mask almost as densely as they have on the pattern. Figure 22 is a scanning electron microscope (SEM) image of the sample shown at 1500 times magnification. This mask breakdown was originally attributed to insufficient thickness. Therefore, the thickness was increased from the original value of 15

to 20 nm. Improvement was observed in the mask's integrity during growth, so it was elected to fix the mask thickness at 20 nm for subsequent samples.

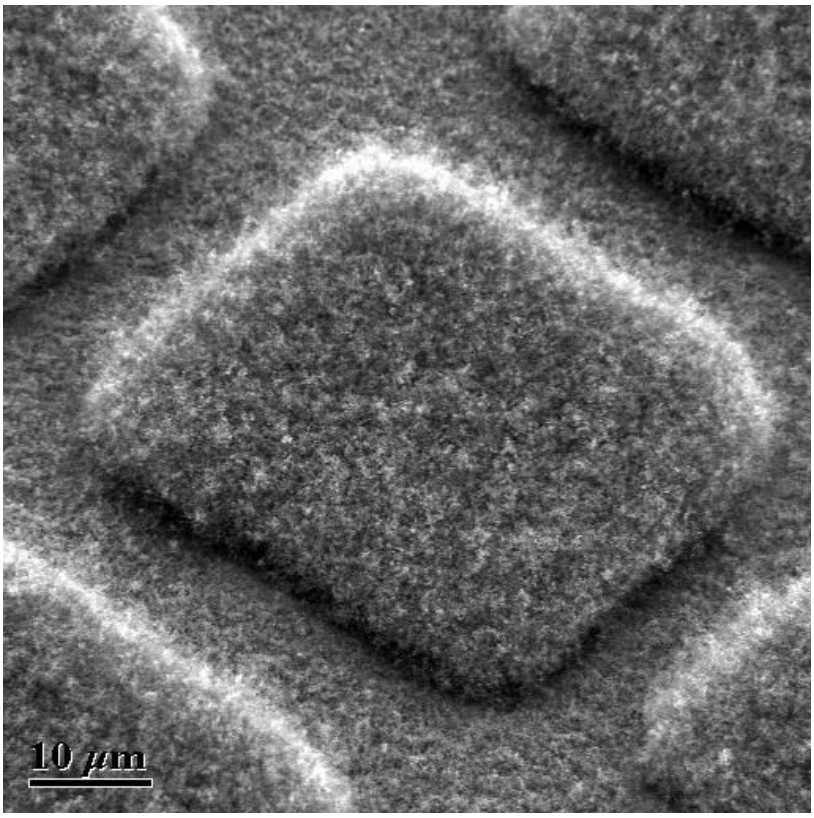

Figure 22. Severe Breakdown of the Molybdenum Mask During CNT Growth (1500x Magnification).

In the samples that followed, mask breakdown was minor, as shown in Figure 23. As can be seen, nanotubes have grown on the mask, though they are of much lower density than those grown on the catalyst layer. Nearby the pillars, there is a region of little to no CNT growth, giving the pillars reasonably good definition. The sample shown in Figure 23 is referred to as Electrode 1 in the remainder of this thesis, because it was the first sample to be of sufficient quality to test in the field emission/ionization chamber (FE/IC).

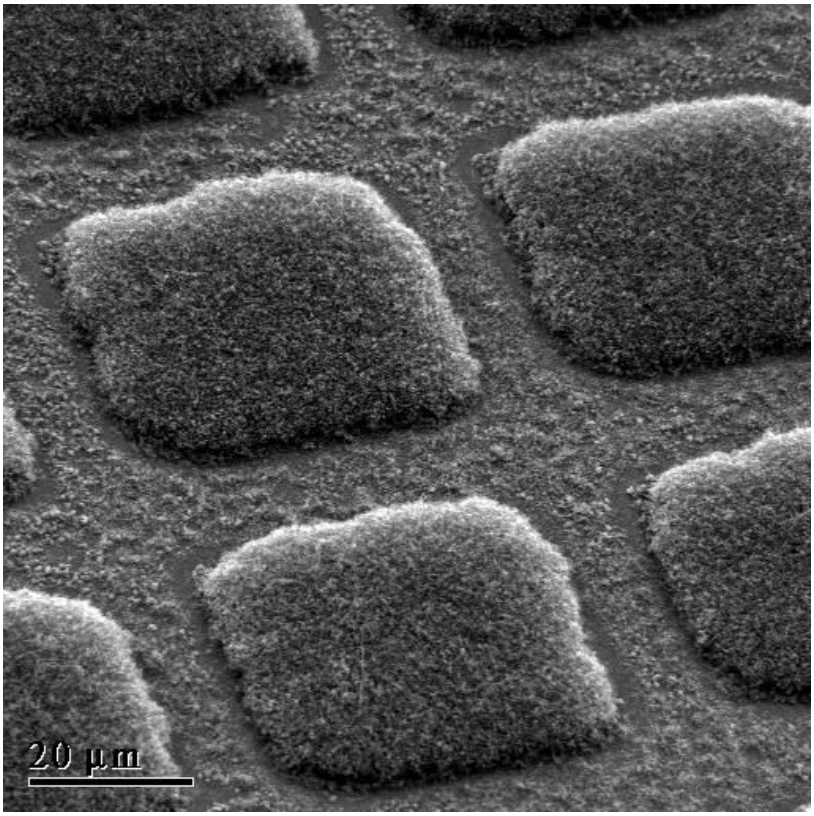

Figure 23. Minor Breakdown of the Molybdenum Mask During CNT Growth (Electrode 1, 1000x Magnification).

The next step in improving the fabrication process dealt with the researchers' suspicion that the ion beam sputterer (IBS) was malfunctioning. One possibility that was considered was that the IBS was drawing insufficient vacuum to prevent oxidation of the metals being sputtered. Since the IBS using ion guns to vaporize metal targets, the metal targets are heated to temperatures high enough to promote rapid oxidation if the vacuum is imperfect, but short of replacing the IBS, there was no way to improve the chamber vacuum. Another possibility was that the crystal detector that senses the thickness of metals deposited was reading incorrectly. This sensor was replaced, but no noticeable improvement was observed in the quality of electrodes fabricated after this replacement. The final possibility for sputtering process error was low purity metal targets. New, high-purity targets were secured, and some improvement in electrode quality was noted.

Following this work on the IBS, the photolithographic process was investigated for areas to improve. All photolithography for this research was performed in the ARC Nanodevice Prototyping Laboratory. The first process error targeted for correction was low pattern resolution. This was the result of two types of procedural errors in the photolithographic process. The first, and less common, error was incomplete photomask contact with the sample. When the photomask is not flat and in uniform contact with the sample, it allows diffraction and shadowing, resulting in poor pattern resolution. The second error was insufficient development of the photoresist. This resulted in a layer of photoresist remaining on the sample, which in turn caused areas of the mask to be lifted off with the pattern during that process step. The result of this damage to the mask was unpatterned, or poorly-patterned, CPA growth. Next, all process chemicals were replaced with new stock. Also, greater time and attention was given to the final inspection of the pattern prior to sputtering the mask. At this stage in the process, a poorly made pattern cannot be corrected, only redone. It does save time, however, to discover the pattern is unacceptable prior to sputtering on the mask versus performing the lift off and finding that the pattern is damaged or nonexistent. Lastly, the cleaning step which follows development was improved by allowing more time to focus on detailed removal of photoresist from the unpatterned areas of the sample while giving greater care to protection of the pattern. In essence, more practice was required for the author to become proficient at the photolithographic process.

Once all of the previous stages were examined and improved, the TCVD process itself was scrutinized. Originally, the gas flow rates for hydrogen (H_2) and ethylene (C_2H_4) were 200 and 800 standard cubic centimeters per minute (SCCM) respectively. This resulted in nanotubes and amorphous carbon being deposited on all areas of the sample. This was evidence of excess carbon; therefore the ratio was changed to 100/270 SCCM of H_2/C_2H_4. With this gas mixture, the deposition of carbon on masked areas was greatly reduced, but was still evident.

Originally, the growth time was set at five minutes, but in an effort to grow denser, longer nanotubes, this was increased in one minute increments, until a growth time of ten minutes was attempted. There were no adverse effects from doubling the growth time, and the nanotubes did exhibit increased density. The final TCVD parameter that was examined was temperature. The standard recipe called for a temperature of 750ºC. Some growths were performed at 760ºC, and while the CNT growth was denser, there was also an increase in mask degradation due to the higher temperature. Growths were also attempted at 745ºC and 740ºC, and the growth at 740ºC resulted in the highest quality sample to that point. It was decided that a calibration of the furnace should be performed, so a stand-alone thermocouple was used to determine the accuracy of the furnace's thermostat. The furnace was turned on and set to 750ºC; it was allowed to stabilize for five minutes after reaching the commanded temperature. At the center of the furnace, where its built-in thermocouple is installed, the stand-alone thermocouple read a temperature of 774ºC. Clearly, this difference in temperature was a very likely contributor to both CNT overgrowth and mask degradation.

A new sample was fabricated with TCVD parameters as shown in Table 1. The resultant electrode was by far the highest quality sample fabricated to that point. As can be seen in Figure 24, the pattern is of very high resolution and the mask is undamaged. The two pillars that appear to be missing or damaged resulted from imperfections in the photomask, not from fabrication errors. Improvements in this stage of the fabrication process realized the greatest improvements in end-state electrode quality. This sample was dubbed Electrode 2.

Set Temperature (ºC)	700
Growth Time (mins)	10
H_2 (SCCM)	100
C_2H_4 (SCCM)	270

Table 1. TCVD Growth Parameters for Electrode 2.

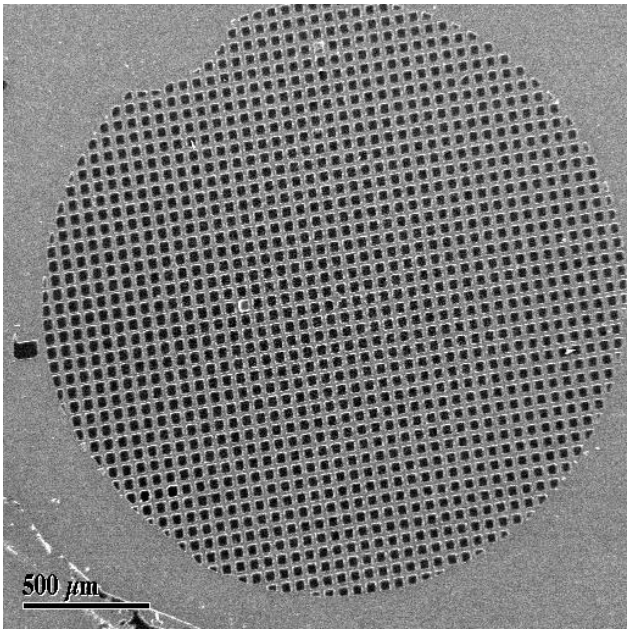

Figure 24. Well-fabricated CPA Electrode (Electrode 2, 40x Magnification).

Looking at Figure 25, this electrode exhibits near-perfect mask integrity. While the CNTs are not as well-aligned as those in Figure 8, they have uniform height and are high-density. The sharper definition of the pillars versus the mask should result in a higher γ.

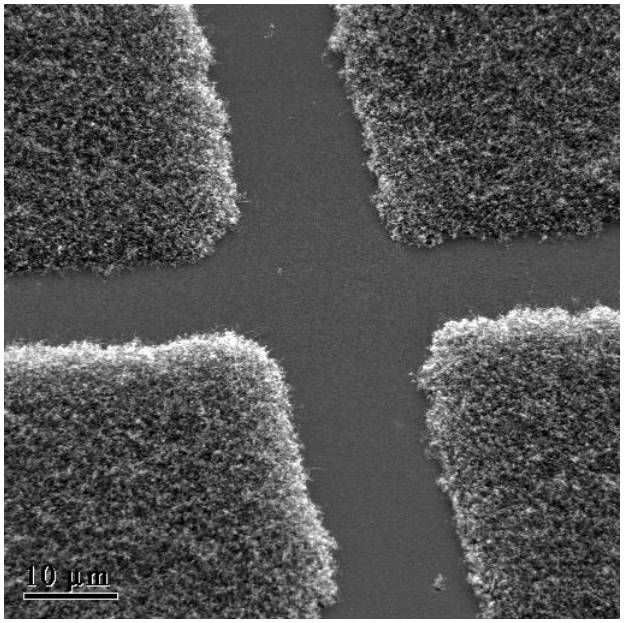

Figure 25. Near-perfect Mask Appearance (Electrode 2, 1000x Magnification).

Following the success of this fabrication, other electrodes were fabricated with small variations in the recipe shown in Table 1. The next sample was fabricated using a set-temperature of 710ºC, but the furnace controller overshot the commanded temperature by eight degrees Celsius, and the result was moderate to severe mask degradation and undesirable CNT growth outside of the patterned area. After that, more attention was given to the furnace controller; with the commanded temperature initially set to 690ºC, or 15ºC lower than the final desired temperature. Once the furnace stabilized at that temperature, the controller was manually stepped up in small increments until the desired temperature of 705ºC was reached. This manual control resulted in temperature overshoots of 0-2ºC, and mask degradation was not observed in these samples. The last two electrodes fabricated, Electrodes 3 and 4, were fabricated according to the recipes shown in Table 2. Electrodes 3 and 4 are shown in Figure 26 and Figure 27. Note in Figure 26 the noticeably longer nanotubes attributable to the doubling of growth time in Electrode 3's fabrication. Notice also the denser growth on Electrode 4. This is most likely due to the fact that Electrode 4 was upstream of the other sample in the RV while Electrode 3 was downstream of its partner in the RV. The result is that Electrode 4 probably had a higher concentration of free carbon to react with its catalytic iron layer than did Electrode 3.

	Electrode 3	Electrode 4
Set Temperature (ºC)	705	705
Growth Time (mins)	10	5
H_2 (SCCM)	100	100
C_2H_4 (SCCM)	270	270

Table 2. TCVD Growth Parameters for Electrodes 3 and 4.

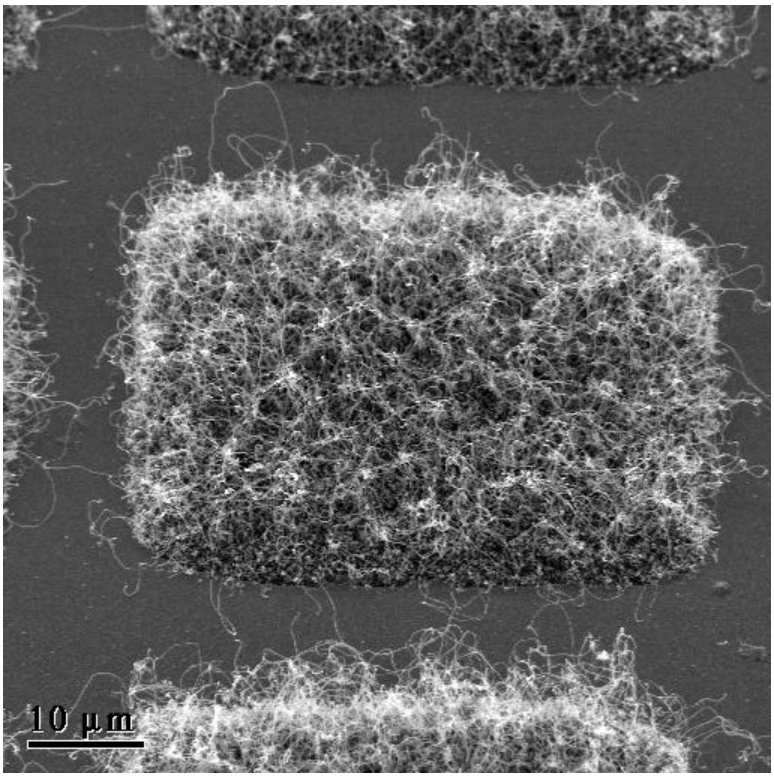

Figure 26. Electrode 3, 1500x Magnification.

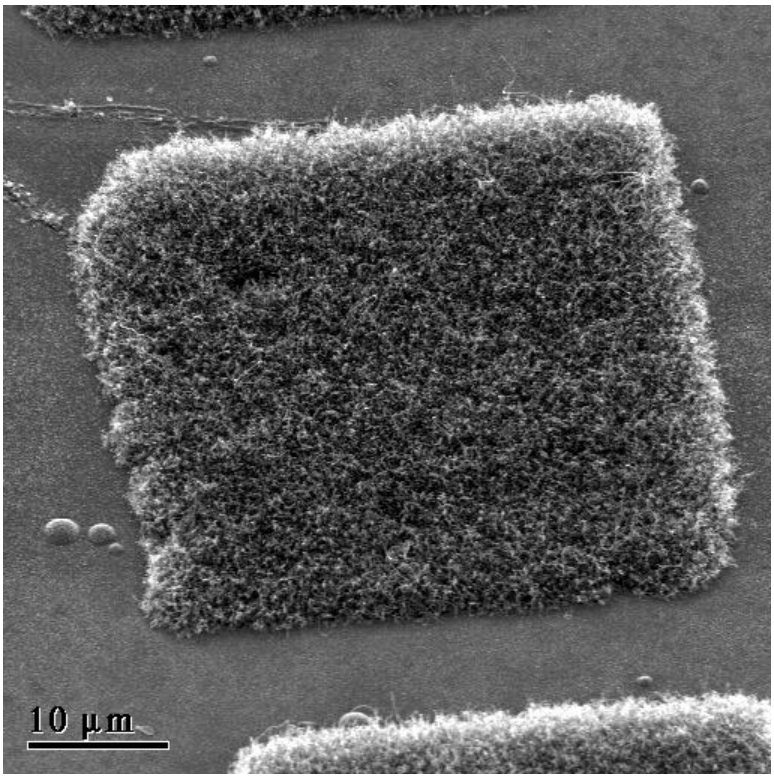

Figure 27. Electrode 4, 1800x Magnification.

B. FIELD EMISSION / IONIZATION CHAMBER AND ASSOCIATED EQUIPMENT

All experimentation on electrodes fabricated for this research was conducted in the FE/IC in the ARC Nanodevice Characterization Laboratory. Figure 28 shows the FE/IC and its associated equipment. Not shown in this figure are the pressure transducer readout, which sits on the workbench to the left of the apparatus, the roughing pump, which is below the test-bench, and the high-voltage source-measurement unit (SMU).

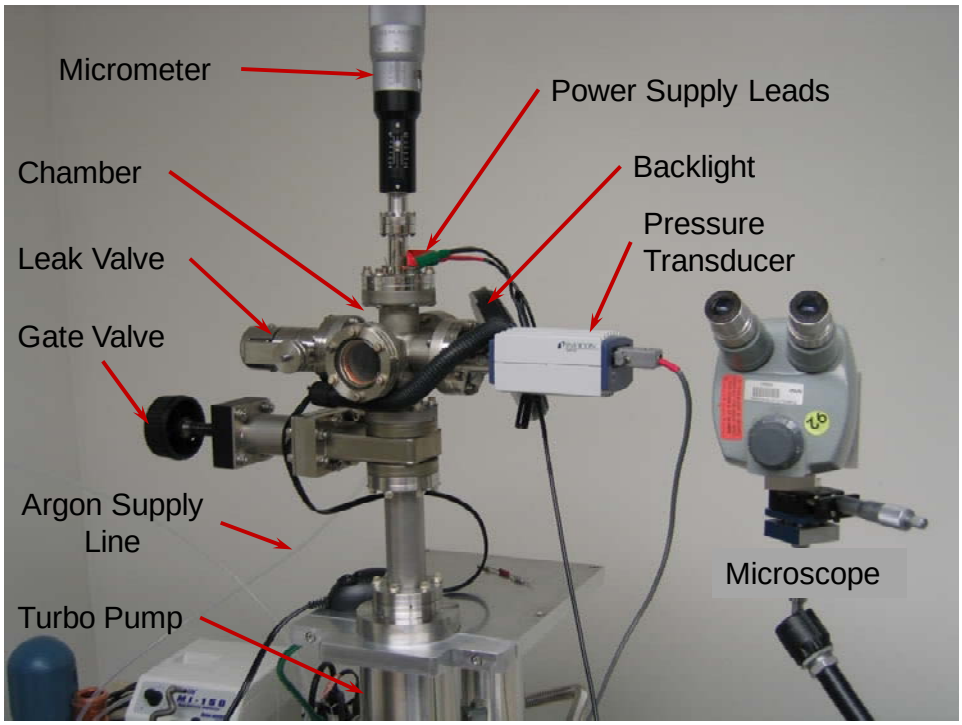

Figure 28. Field Emission/Field Ionization Chamber and Associated Equipment.

The FE/IC is a precision instrument, capable of achieving vacuum levels as high as 10^{-9} Torr. Consequently, it requires care whenever samples are loaded or unloaded, or any time the chamber configuration is altered. Detailed procedures for loading electrodes into the FE/IC are found in Appendix A, Section E. As shown in Figure 28, the FE/IC was configured with a gate valve to isolate the chamber from the turbo pump. This was intended to allow the

chamber to be stabilized at a constant argon pressure, while not overstressing the turbo pump. Unfortunately, the gate valve, being new, continued to out-gas throughout the course of the experiments. This precluded isolating the chamber because the out-gassing rapidly raised the pressure in the chamber whenever the gate valve was closed. For this reason, the gate valve was left fully open for the duration of the experiments.

The other item to note is the leak valve. The valve pictured in Figure 28 is the second leak valve installed during the course of these experiments. The first leak valve installed was found to not hold vacuum higher than 10^{-4} Torr. Investigation showed that this valve's specified leak rate and maximum input pressure combined to give it an expected ability to maintain only 10^{-4} Torr on the outlet. Therefore, a second valve was purchased with a specified leak rate of 10^{-10} Torr, which was more than sufficient to maintain the chamber at any vacuum level desired during these experiments.

Once connected to the FE/IC, this leak valve was used to adjust the chamber pressure by introducing high-purity (99.999%) argon until the pressure display showed the desired partial pressure of argon. It was assumed that, because the chamber was evacuated to better than $5x10^{-7}$ Torr prior to any experiments, the pressure displayed on the readout was due overwhelmingly to the argon, and that residual non-argon components of the chamber environment were negligible.

The other major component of the test apparatus was the Keithley 237 high-voltage SMU. The SMU comprises four instruments, namely a voltage source and measurer, and a current source and measurer. The SMU is rated to have a current measurement sensitivity of 10 femtoamperes and a voltage measurement sensitivity of 10 μV. It has a maximum output of 1100 V and a sampling rate of up to 1000 measurements per second. It is capable of outputting various waveforms, but the two of interest to this research were the fixed level and the linear stair.

The SMU was connected directly to the test apparatus with alligator clamps, but was controlled by the Laboratory Virtual Instrument Engineering Workbench (LabVIEW). The SMU's data output was also routed to LabVIEW for storage and viewing.

THIS PAGE INTENTIONALLY LEFT BLANK

IV. EXPERIMENTAL RESULTS

A. SETUP AND PROCEDURES

1. Electrode Characterization

A simple characterization must be performed prior to loading a sample electrode into the FE/IC. The resistance between the surface of the lower electrode and its respective lead must be measured. The results of this measurement for the four electrodes tested are shown in Table 3.

Electrode	Lead-to-Electrode Resistance
1	100 Ω
2	980 Ω
3	67 Ω
4	86 Ω

Table 3. Lead-to-Electrode Resistance Values for Tested Electrodes.

2. Electrode Landing

The first step in testing a sample electrode is to land the upper electrode on it, in order to positively determine the zero-gap position from which all test gaps are measured. To do this, the current versus time graph is enabled on LabVIEW, and the SMU is configured via LabVIEW as shown in Table 4.

Voltage Limit	1 V
Compliance	4E-4 A
Waveform	Fixed Level
Voltage	1 V
Measurements	10000
Delay	20 ms

Table 4. SMU Parameters for Electrode Landing.

Using the microscope, the upper electrode is moved to be very close to, but still visually separated from, the test sample. After starting LabVIEW, the micrometer is turned slowly until contact is made between the electrodes, as signified by a significant jump in current. The micrometer reading at contact is noted, then the micrometer is backed off to the desired initial test gap, usually 10μm. The LabVIEW output of a landing is shown in Figure 29.

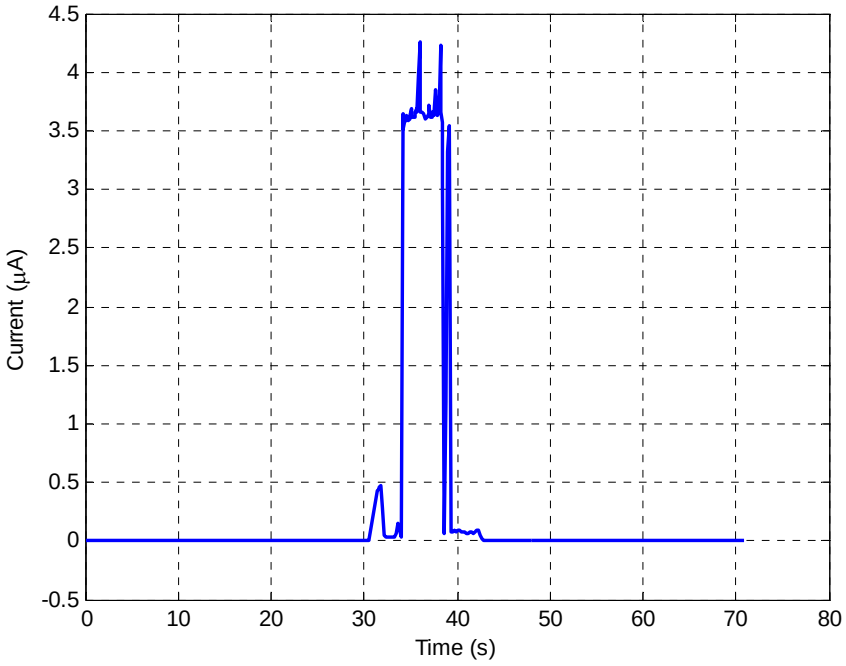

Figure 29. Plot of Current vs. Time Used to Determine Anode-Cathode Landing.

3. Field Emission / Field Ionization Tests

To prepare for collecting data, a few critical items must be checked. First, ensure only the Keithley 237 is active. Next, check that LabVIEW is programmed to operate the SMU within the desired parameters. Prior to collecting data, the electrode must be conditioned. Conditioning the electrode involves conducting multiple test runs at the initial test gap until the electrode exhibits consistent performance in terms of turn-on voltage and compliance voltage. LabVIEW should be set to display the current versus voltage graph (I-V plot). The SMU should be set as shown in Table 5. The SMU is started via LabVIEW, and

sweeps from the start voltage to the end voltage in steps of a size determined by the voltage range divided by the number of desired measurements. In all of these experiments, the SMU was programmed in such a way as to collect data in one volt increments.

Voltage Range	1100 V
Waveform	Linear Stair
Start Voltage	0 V
End Voltage	1100 V
Compliance	4E-4 A
Measurements	1100
Delay	4 ms

Table 5. SMU Parameters for Field Emission/Ionization Testing.

B. ELECTRODE 1

The experiments on Electrode 1 were conducted under ultrahigh vacuum (UHV) with a base pressure of 2.7×10^{-7} Torr. At the time of this experiment, Electrode 1 was the only sample which had been fabricated with sufficient quality to be deemed testable. For this reason, the tests on Electrode 1 were much less ambitious than tests on follow-on samples. Electrode 1 was only connected as a cathode in a diode configuration. The compliance was set to 10 μA and the voltage was limited to 250 V. Furthermore, as previously discussed, the leak valve which was installed was found to be incapable of holding the desired vacuum, so no static argon testing was conducted on Electrode 1. Consequentially, Electrode 1 was only operated as a field electron emitter, not as a field ionizer.

Initially, the electrode gap was set at 10 μm, and the electrode was conditioned. Then, data runs were conducted, three per gap setting, at gaps ranging from 10 to 70 μm in 10 μm increments. The data from those runs were

averaged to produce the plot shown in Figure 30. The reason for averaging multiple data runs is to smooth sensor anomalies and noise, producing a more representative characterization curve.

For the purposes of this thesis, turn-on voltage is defined as that voltage required to generate 1 μA of current. For Electrode 1, at a 10 μm gap, the turn-on voltage was 115 V, which equates to an average electric field of 11.5 V/μm (see Appendix B, Table 7), a value that agrees with previous studies. At higher gap settings, the applied field was observed to be as low as 4.7 V/μm. The I-V plot for all gaps tested is shown in Figure 30. Also shown in Figure 30 is the fact that Electrode 1 never turned on at gap settings greater than 50 μm because of the voltage limit programmed in the SMU. Also of interest is the decrease in the average electric field necessary to achieve turn-on as the electrode gap is increased.

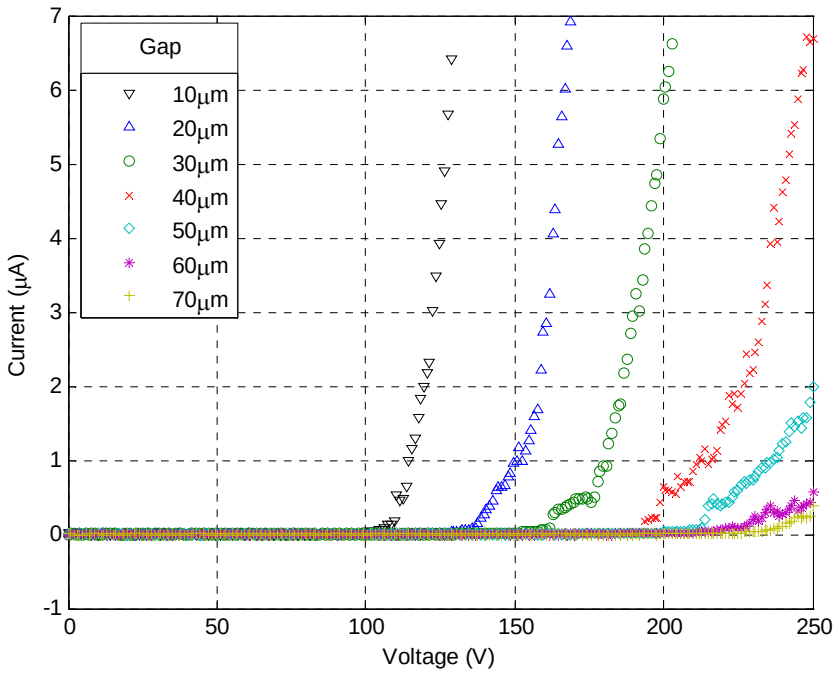

Figure 30. I-V Plot for Various Interelectrode Gaps (Electrode 1, UHV).

C. ELECTRODE 2

The first round of experiments on Electrode 2 was conducted under UHV with a base pressure of 2.4×10^{-7} Torr. For this round, Electrode 2 was connected as a cathode in a diode configuration. The compliance was calculated to meet the desired current density of 10 mA/cm^2. Since the CPA is 2 mm in diameter, its area is 0.0314 cm^2. This means that the desired current density requires a current of 0.314 mA. To ensure some margin above this, the SMU was programmed with a compliance of 0.4 mA.

Initially, the electrode gap was set at 10 μm, and the electrode was conditioned. Then, data runs were conducted, three per gap setting, at gaps ranging from 10 to 60 μm in 10 μm increments. The data from those runs were averaged to produce the plot shown in Figure 31. Data runs were also conducted at 70 μm, but the electrode did not achieve the targeted current density prior to the SMU reaching its upper voltage limit.

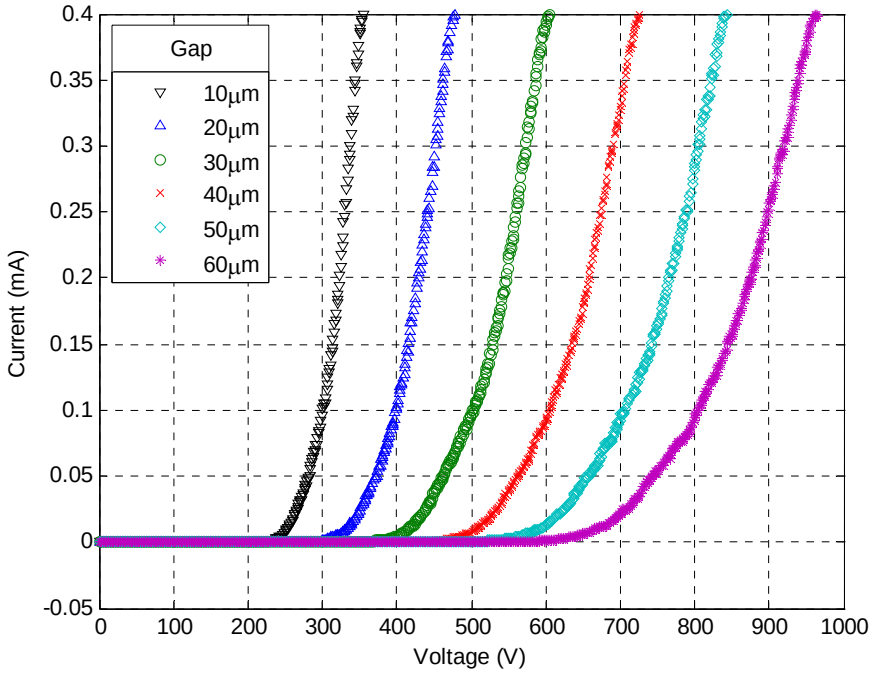

Figure 31. I-V Plot for Various Interelectrode Gaps (Electrode 2, UHV).

Following the field emission testing at UHV, argon was introduced via leak valve until the chamber pressure stabilized at 2.4×10^{-6} Torr. Field emission data was then collected in a series of runs and averaged, as with the UHV experiments. All of these runs were conducted using an electrode gap of 10 µm. Following the experiments at this pressure, data runs were performed at pressures from 2.4×10^{-5} to 2.4×10^{-2} Torr. These data are shown in Figure 32. Of special interest is the data collected at 2.4×10^{-2} Torr. The data gives strong evidence of microarcing and electrode damage. This was confirmed when the electrode was removed from the FE/IC and examined. The damage is very evident in the SEM images shown in Figure 33 and Figure 34

.

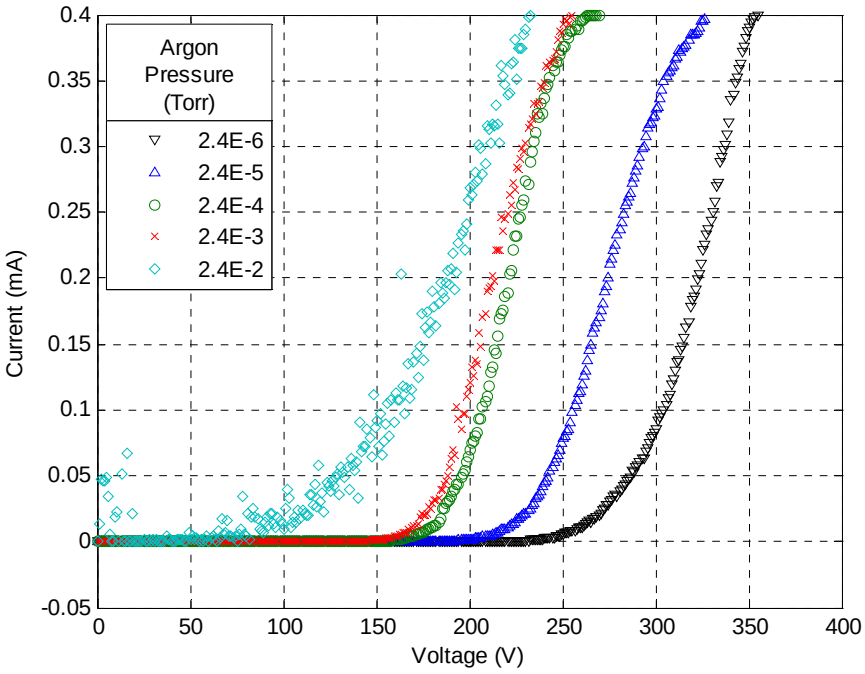

Figure 32. I-V Plot for Field Emission at Various Argon Pressures (Electrode 2, 10µm Gap, Static Argon).

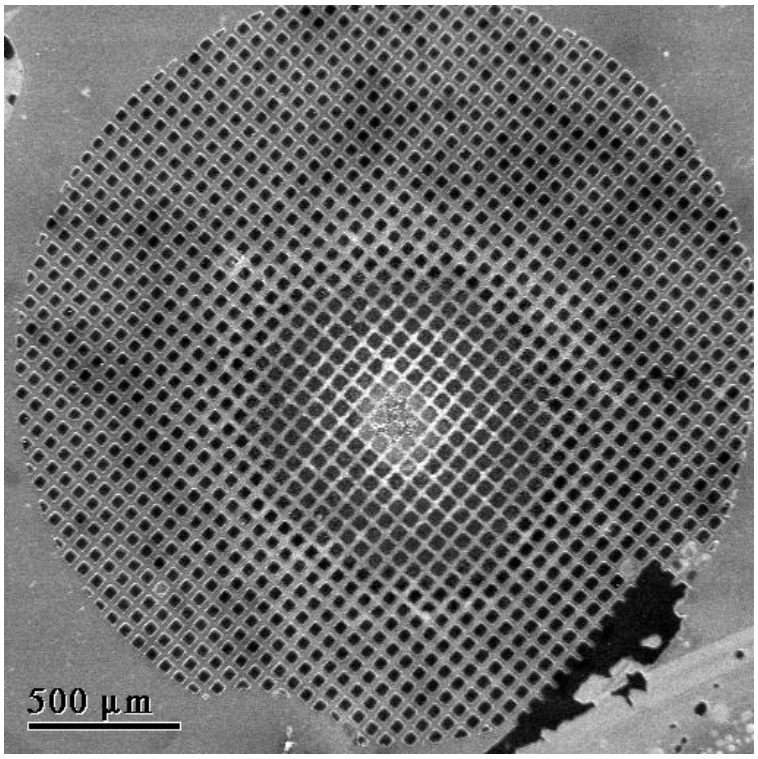

Figure 33. Microarc Damage to the CPA (Electrode 2, 40x Magnification).

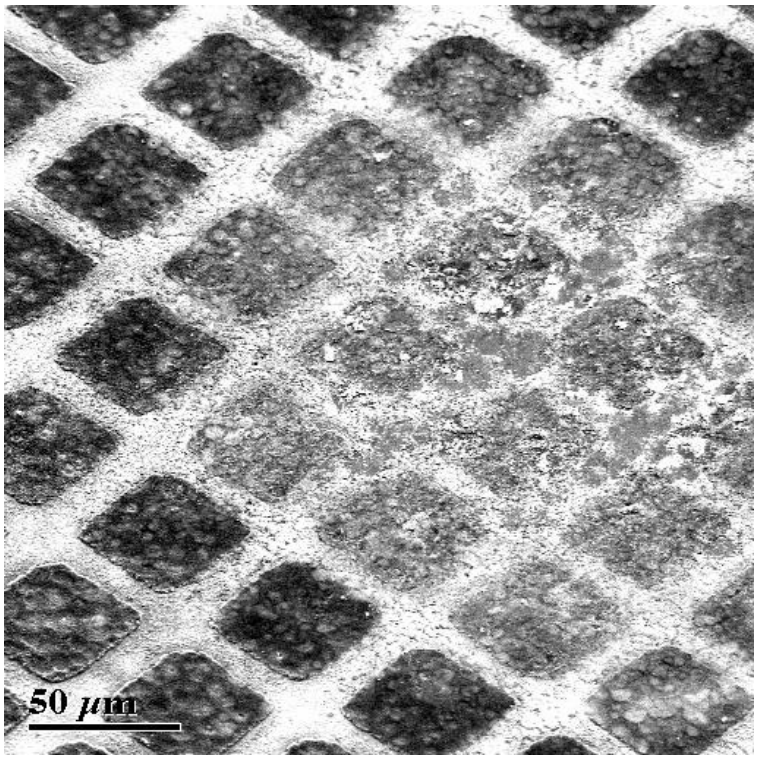

Figure 34. Microarc Damage to the CPA (Electrode 2, 400x Magnification, 45º Tilt).

D. ELECTRODE 3

The first round of experiments on Electrode 3 was conducted under UHV with a base pressure of 4.3×10^{-7} Torr. For this round, Electrode 3 was connected as a cathode in a diode configuration. The SMU was again programmed with a compliance of 0.4 mA. The same data runs were collected for Electrode 3 as were for Electrode 2, with the exception that compliance was achieved at a gap of 70 μm. These data are shown in Figure 35.

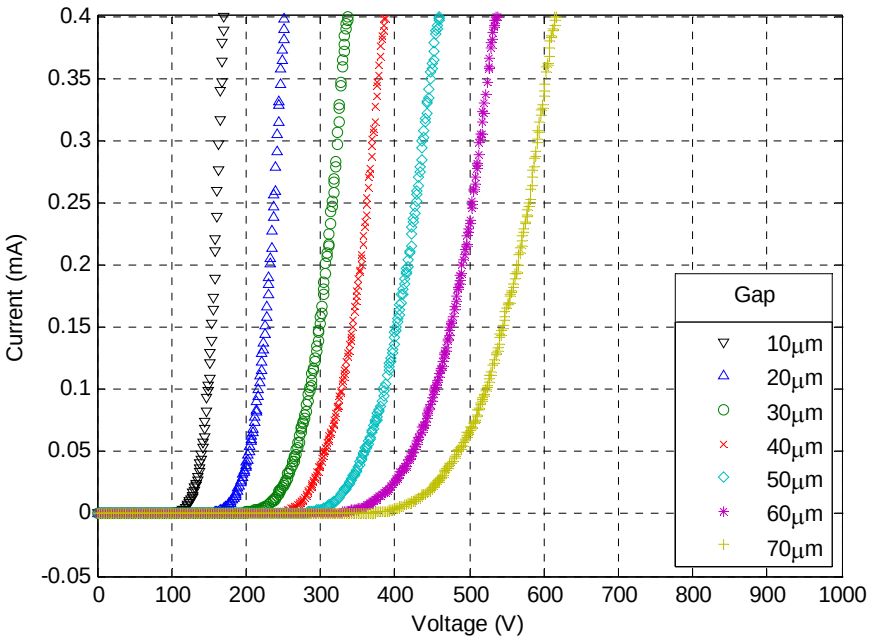

Figure 35. I-V Plot for Various Interelectrode Gaps (Electrode 3, UHV).

Following the field emission testing at UHV, the sample was reconfigured as an anode to conduct field ionization testing. Argon was introduced via leak valve until the chamber pressure stabilized at 2.2×10^{-6} Torr. Field ionization data was then collected as previously described. All of these runs were conducted using an electrode gap of 50 μm to prevent the microarcing which was observed during experiments on Electrode 2. Following the experiments at this pressure, data runs were performed at 2.2×10^{-5} and 2.2×10^{-4} Torr. No higher pressures were attempted, again in order to preserve the electrode. These data are shown

in Figure 36. As can be seen, the runs at $2x10^{-6}$ Torr were without incident, being smooth and exhibiting turn-on voltage in the expected range (350-450 V). Evidence of microarcing did, however, begin to be observed at high voltages for argon at $2x10^{-5}$ Torr. Even with apparent damage to the electrode, it continued to produce consistent performance at currents below approximately 50 μA.

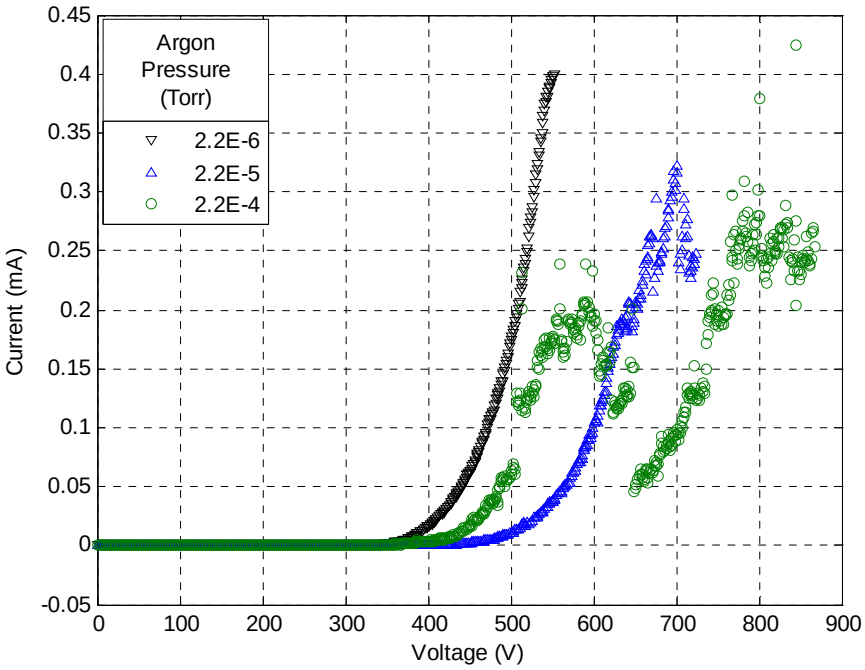

Figure 36. I-V Plot for Field Ionization at Various Argon Pressures (Electrode 3, 50μm Gap, Static Argon).

Finally, Electrode 3 was reconfigured for field emission and was tested in argon environments ranging from $2.2x10^{-6}$ to $2.2x10^{-4}$ Torr. These data are shown in Figure 37. Despite apparent damage from the field ionization experiments, Electrode 3 required only slightly higher turn-on fields and exhibited consistent performance throughout numerous repeated data runs.

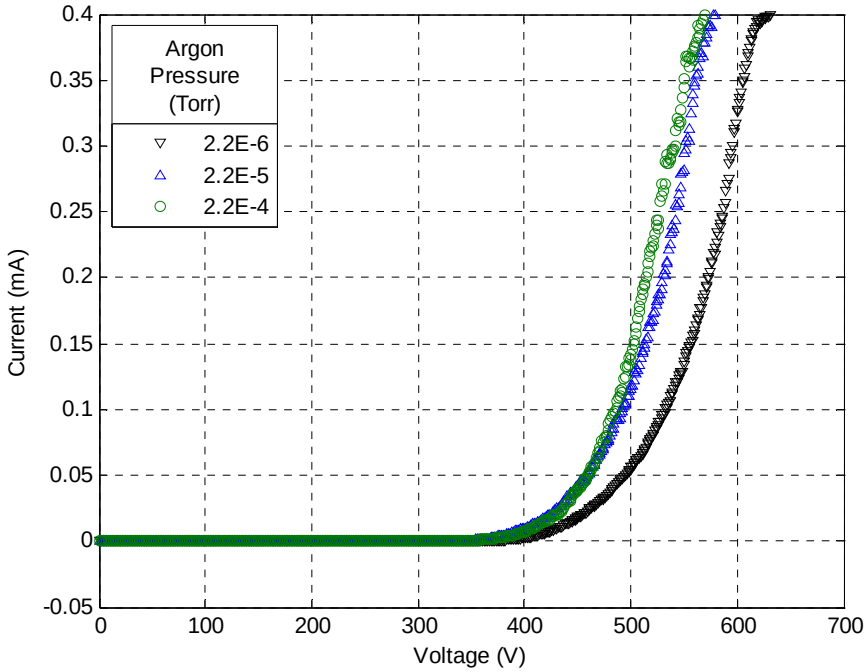

Figure 37. I-V Plot for Field Emission at Various Argon Pressures (Electrode 3, 50μm Gap, Static Argon).

The final characterization made of Electrode 3 involved its compliance with the Fowler-Nordheim (F-N) model for field emission. The F-N model describes the relationship between current, voltage and the work function. For this thesis, a work function of 5 eV was assumed in all cases. The Fowler-Nordheim equation is given as

$$I = \left(\frac{q^3}{8h\pi\phi} \right) V_t^2 \exp\left(-\frac{8\pi\sqrt{2m}\phi^{\frac{3}{2}}}{3hqV_t} \right) \tag{6}$$

where I is the current, V_t is the voltage at the emitting tip, h is Planck's constant (4.136E-15 eV·s), ϕ is the aforementioned work function, m is the electron mass (9.109E-31 kg), and q is the elementary charge (1.602E-19 C) [11]. However, the F-N equation assumes a number of unrealistic features. Subsequent work has produced a modified F-N equation with correction for the image charge

smoothing of the potential barrier. This modified F-N equation incorporates the elliptical emission functions approximated by the expressions shown in equations (7) and (8).

$$t(y) = 1 + 0.1107\,y^{1.33} \tag{7}$$

$$v(y) = 1 - y^{1.69} \tag{8}$$

where

$$y = \frac{1}{\phi}\sqrt{\frac{q^3 V_t}{4\pi\varepsilon_0}} \tag{9}$$

where ε_0 is the vacuum permittivity (8.854E-12 F/m). Incorporating fitting parameters, and assuming $t(y)$ and $v(y)$ to be very close to 1, a further-modified F-N equation is derived and shown in equation (10),

$$I = \left(\frac{2\pi r^2 A}{\phi}\right) V_t^2 \exp\left(-\frac{B\phi^{\frac{3}{2}}}{V_t}\right) \tag{10}$$

where A = 1.541x10^{-6} A·eV/V^2 and B = 6.831x10^9 V/(eV$^{3/2}$·m) [19]. Rearranging equation (10) gives

$$\frac{I}{V_t^2} = \left(\frac{2\pi r^2 A}{\phi}\right) \exp\left(-\frac{B\phi^{\frac{3}{2}}}{V_t}\right) \tag{11}$$

and taking the natural logarithm of both sides gives

$$\ln\left(\frac{I}{V_t^2}\right) = \ln\left(\frac{2\pi r^2 A}{\phi}\right) + \left(-\frac{B\phi^{\frac{3}{2}}}{V_t}\right) \tag{12}$$

which, setting $V_t = \beta V_a$,where V_a is the applied voltage, becomes

$$\ln\left(\frac{I}{V_a^2}\right) = \ln\left(\frac{2\pi r^2 A}{\phi}\right) + \left(-\frac{B\phi^{\frac{3}{2}}}{\beta V_a}\right) \tag{13}$$

Lastly, setting $1/V_a = x$ gives

$$y(x) = \ln\left(\frac{2\pi r^2 A}{\phi}\right) + \left(-\frac{B\phi^{\frac{3}{2}}}{\beta}\right)x \tag{14}$$

where β is the geometric field enhancement factor. Equation (13) then, is of the form $y = mx + b$, a simple line. By taking linear fits of the data using MATLAB, the slope of the fit can be used to calculate β directly. Since

$$\gamma = \beta\lambda \tag{15}$$

where λ is the electrode gap, γ can be calculated from these data fits as well. The γ for Electrode 3 prior to field ionization was 1100, and after field ionization, 840, a reduction of approximately 24%. The comparison of the field emission performance of Electrode 3 to the theoretical performance as determined by the F-N equation is shown in Figure 38.

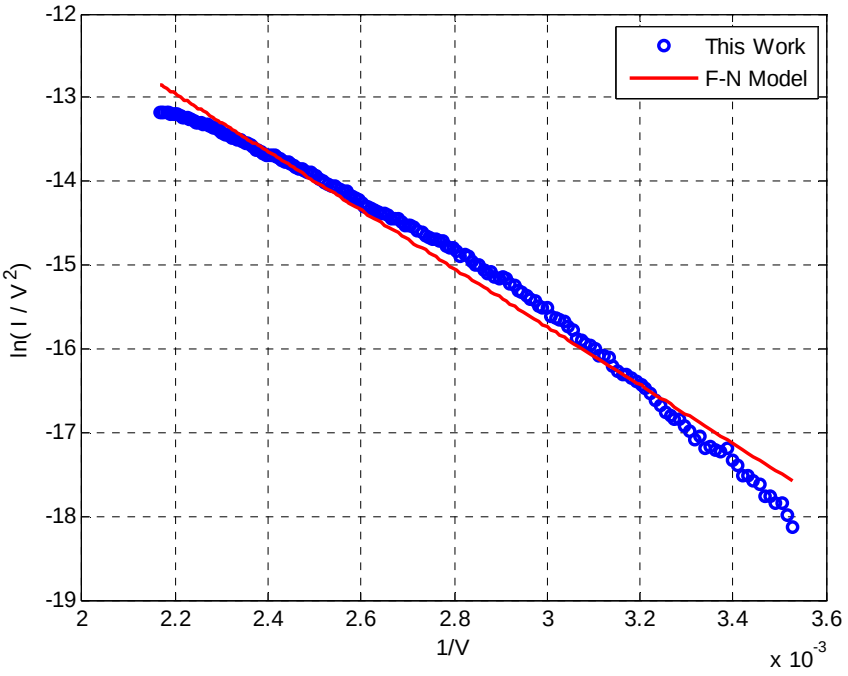

Figure 38. Fowler-Nordheim Plot for Field Emission (Electrode 3, 50μm Gap, UHV).

After testing was complete, Electrode 3 was reexamined with the SEM. The result is shown in Figure 39. The damage to the array was most likely caused by the upper electrode not being perfectly flat and/or not being parallel to the lower electrode. Either of these can cause hotspots in the array, resulting in the burnout damage seen in Figure 39. The damage appears extensive, with a circular area approximately half the diameter of the array flattened. This corresponds to an area approximately one-quarter that of the array, which correlates with the previously calculated reduction in γ. Despite this damage and reduction in performance, the array continued to produce smooth I-V curves and to achieve compliance current densities.

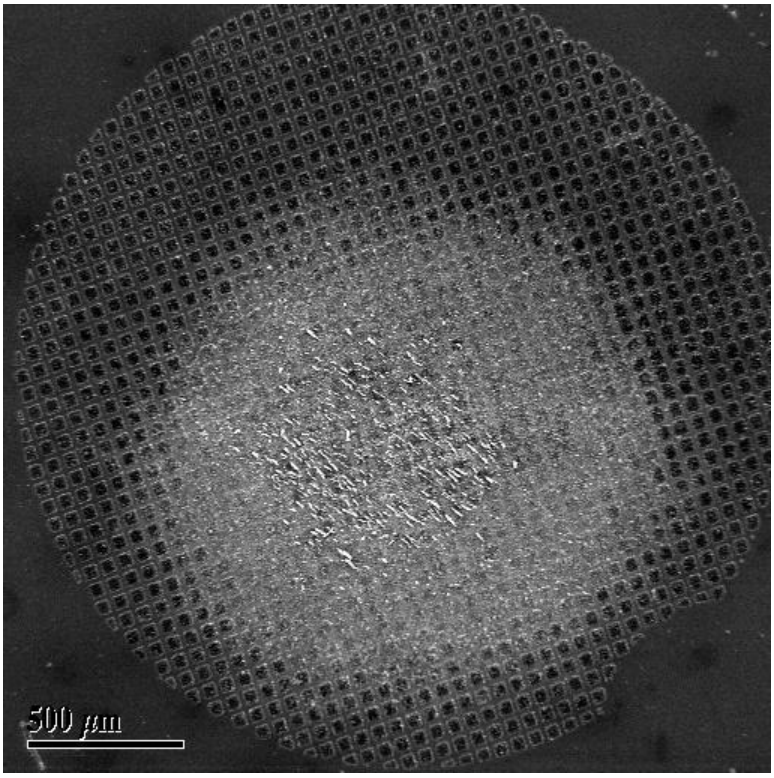

Figure 39. Post-experimentation Image of Electrode 3 (40x Magnification).

E. ELECTRODE 4

Electrode 4 was tested identically to the methods described for Electrode 3, with the exception that the vacuum pressure was 2.6×10^{-7} Torr. The data are included in Figure 40, Figure 41 and Figure 42 for completeness. The first item to note is that Electrode 4's turn-on voltages at small gaps are the lowest of any electrode tested to date. Second, there is erratic behavior in the field ionization regime even at an argon pressure of only 2×10^{-6} Torr, but this is balanced by the fact that the performance is smooth up to 100 μA, or double the current that Electrode 3 could reliably produce. Lastly, note in Figure 40 and Figure 42, the slope of the curves is the sharpest yet observed, indicating Electrode 4 should exhibit the highest γ, and indeed, the γ for Electrode 4 prior to field ionization was 1440. The most surprising result, however, was that after field ionization, γ for Electrode 4 was 1510, an increase of approximately 5%. Looking at Figure 43, it

can be seen that nearly the entire area of the electrode has been altered by the experiment. It is likely that this resulted in a flattening of the electrode, creating a more uniform array which, as previously discussed, results in more even field distribution. This in turn increases the CPA performance, as measured by γ. The comparison of the field emission performance of Electrode 4 to the theoretical performance as determined by the F-N equation is shown in Figure 44. This figure reinforces the conclusion that Electrode 4 was the best-performing electrode fabricated during this research.

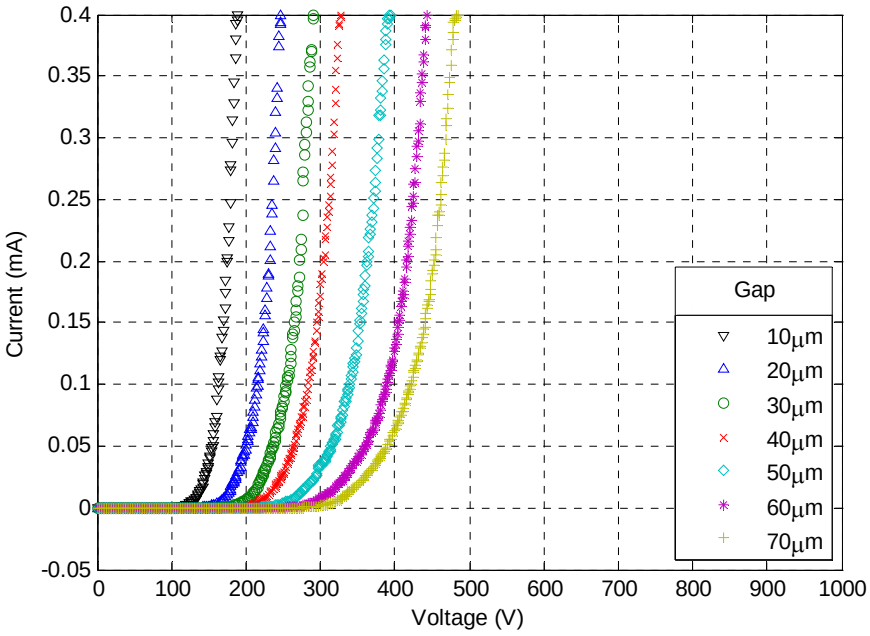

Figure 40. I-V Plots for Various Interelectrode Gaps (Electrode 4, UHV).

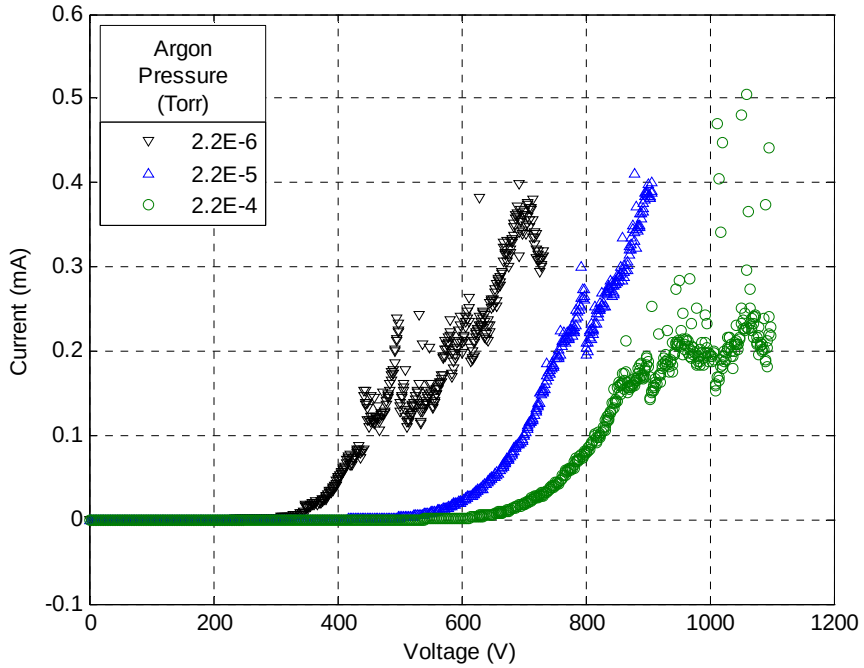

Figure 41. I-V Plot for Field Ionization at Various Argon Pressures (Electrode 4, 50µm Gap, Static Argon).

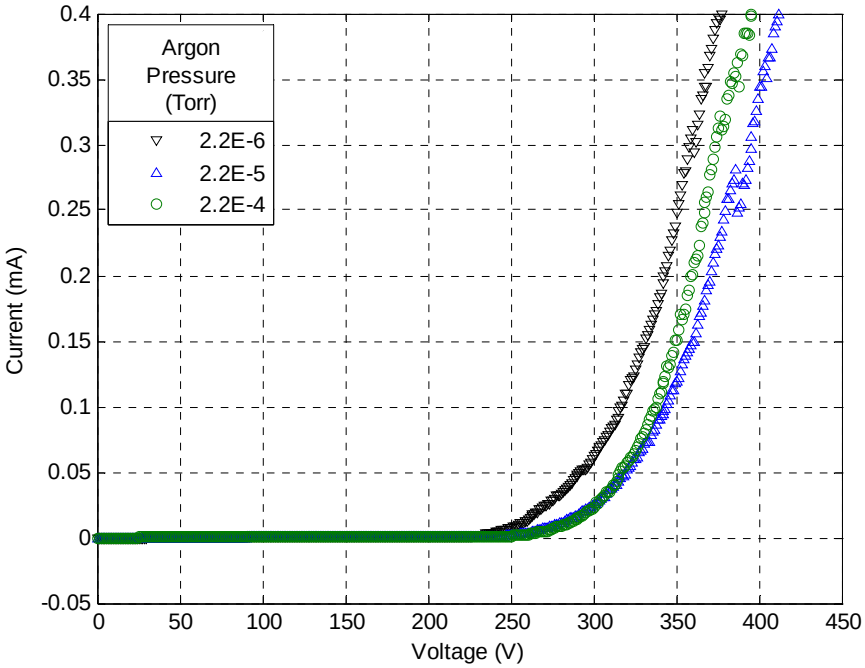

Figure 42. I-V Plot for Field Emission at Various Argon Pressures (Electrode 4, 50µm Gap, Static Argon).

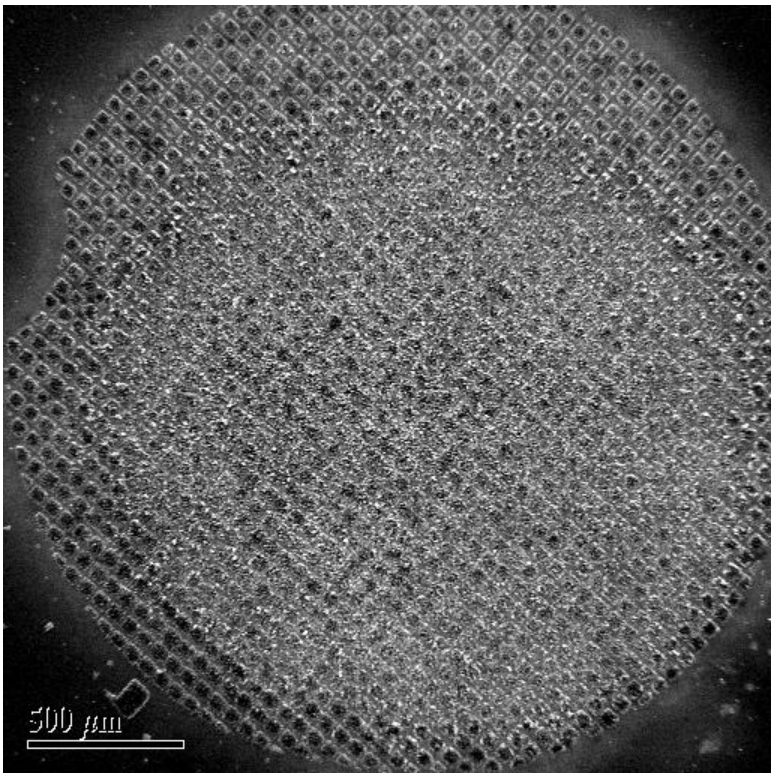

Figure 43. Post-experimentation Image of Electrode 4 (40x Magnification).

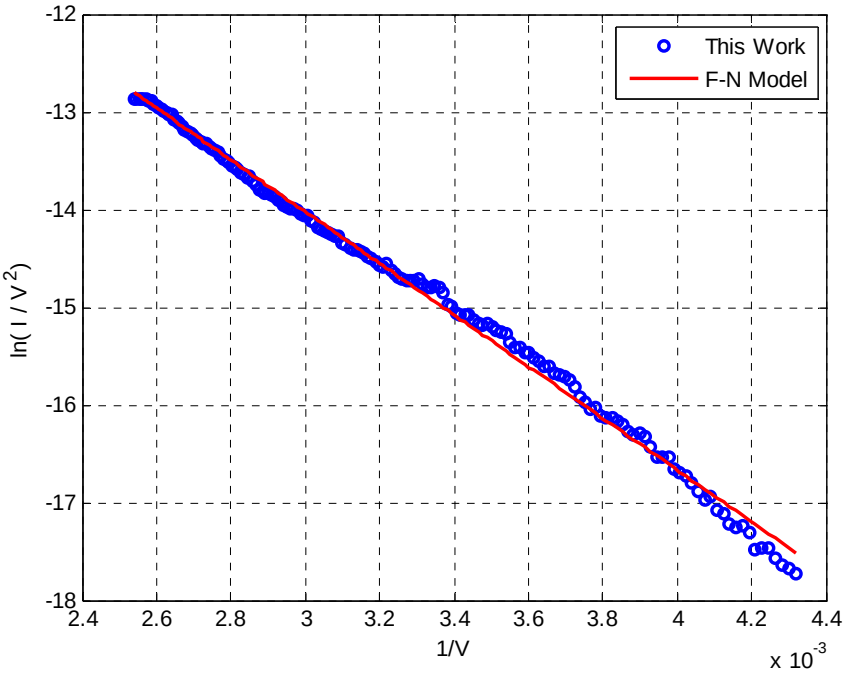

Figure 44. Fowler-Nordheim Plot for Field Emission (Electrode 4, 50µm Gap, UHV).

The field enhancement factors for all four electrodes tested during the course of this research are summarized in Table 6.

.

Electrode	γ Prior to Field Ionization	γ After Field Ionization
1	900	N/A
2	570	N/A
3	1100	840
4	1440	1510

Table 6. Summary of Field Enhancement Factors for Electrodes 1-4.

Tabulated data for turn-on voltage and compliance voltage, for both UHV and static argon environments of various pressures, for all four electrodes tested during this research are found in Appendix B.

V. CONCLUSIONS AND RECOMMENDATIONS

A. SUMMARY

Most current propulsion devices are not compatible with the volume and mass constraints of small satellites. Due to their size, small-sats require very compact, high efficiency propulsion systems. Electric propulsion, specifically the ion electrostatic thruster, is one of the best candidates to meet these requirements, but current ion sources in these thrusters are not scalable. A new, efficient and scalable ion source is being researched.

At the outset of this thesis, it was envisioned that a flow-through CPA electrode would be fabricated, tested and characterized for its suitability as a miniature scalable field ionizer. Obstacles to successful perforation of the substrate prevented meeting this goal. Other difficulties in the fabrication process were also encountered; especially hindering to the research was the time-consuming process of troubleshooting the TCVD process. Near the end of the research period, however, there were great improvements made in the fabrication process, and four electrodes were produced of sufficient quality to warrant experimentation. The correct components were on hand, or able to be acquired quickly, and the FE/IC was configured to support both field emission and field ionization testing.

The experimentation phase of this research produced very exciting results. CPA electrodes were fabricated that exhibited turn-on voltages on the order of 100 V and turn-on applied fields as low 4.13 V/μm. Operated as gas field ionizers, the electrodes exhibited turn-on voltages as low as 263 V, equating to an applied field of only 5.25 V/μm. Current densities greater than 10 mA/cm^2 were achieved, indicating CPA electrodes as small as 2 mm in diameter can indeed produce ion currents of useful amperage at applied electric fields of just a few volts with argon pressures on the order of 10^{-6} Torr. Higher argon pressures tended to result in microarcing, however this may be mitigated by lowering input

voltages. The electrodes tested were each capable of reproducible performance throughout multiple trials and configuration changes. Also notable were the similarities between the γ values of Electrodes 3 and 4, as well as their performance characteristics, indicating that the fabrication process, once standardized, will be capable of producing electrodes that will perform within a small, known envelope.

B. CONCLUSIONS

CPA electrodes are highly efficient field electron emitters and field gas ionizers. They are also robust and reliable devices. Despite apparently severe damage to the array, our tested electrodes repeatedly operated at high current densities while exhibiting consistent performance characteristics. Their key performance metric, γ, was affected by this damage, but not to such an extent as to render them inoperable.

Avoiding similar damage to future electrodes will require a gated extractor electrode being integrated onto the CPA. This should permit even higher current densities with significantly less damage to the structure. If it is desired to fix the current level, a larger CPA or an array of CPAs can easily be fabricated and customized to the parametric requirements of the application.

The CPA electrodes produced during this research hint at the promise of a compact ion source for propulsion that is low in mass and volume, requires very low power to operate and which is fully scalable. This opens the door for future research to explore the production of a miniature ion thruster incorporating a CPA ion source. Since CPAs can also perform as miniature electron sources, there may be applications for them in miniaturizing and reconfiguring the neutralizing cathode as well. As satellites shrink from many thousands of kilograms to just one or two kilograms squeezed into a package barely 1000 cm^3 in size, CPA ionizers could very well be a key component of the ion propulsion systems that will maneuver them, fly them in formation, dock them and keep them space-borne.

C. RECOMMENDATIONS FOR FUTURE WORK

1. Advanced Fabrication Methods and Process Improvement

The first, and most important, follow-on work in this research area must be to perfect the process by which CPA electrodes can be reliably reproduced with minimal variability in their properties. This will involve scrutinizing each step of the process for possible improvements, trying new types and thicknesses of adhesion, catalyst and masking metals, and experimenting with different times, temperatures and gas concentrations during the growth process. Being able to build electrodes with CPAs of consistent height and density means their electrical characteristics and performance will be nearly identical and therefore predictable. This predictability will in turn enable tailoring of designs to specific propulsion applications. Consistent and well-known performance is also essential to the implementation of these devices.

Following the optimization of the basic construction techniques, the processes and procedures for etching the silicon substrate must be perfected. In order to investigate the full potential of CPA ionizers, the next step must be the fabrication and testing of a flow-through electrode. This requires etching a pattern of flow orifices through the substrate. Various methods exist for doing this, including the wet etching technique attempted during this research, as well as dry etching methods such as deep reactive ion etching (DRIE).

The final area of manufacturing and process that should be investigated is in the patterning of the electrode. Of particular interest is nanoimprint lithography, a process whereby the desired pattern of catalytic metal is printed directly on the substrate instead of using the more labor-intensive process of photolithography described in Appendix A, Section C. If nanoimprint lithography is deemed infeasible, higher-resolution photomasks should be acquired or fabricated.

2. Material Studies

This thesis deals exclusively with CNTs, but there are other materials that can be used to create field-enhancing structures. Notably, the previously discussed RPI research using tungsten nanorods showed them to be very robust and suitable as miniature ionizers. Tungsten nanorods also exhibit a material characteristic in the way in which their tips are formed. They terminate in pyramidal apexes, giving them extremely sharp tips, sharper even than the Buckey-ball tips found in CNTs. This sharpness contributes to the tungsten nanorods' high γ. Other materials should be investigated for their suitability as nanorod or nanotube field enhancers.

3. Geometric Design Studies

All of the electrodes built for this research shared a single geometry, as previously discussed. There are, however, a multitude of variables in the array design which can be manipulated toward improving electrode performance. The first of these geometric design variables is pillar shape. Current masks available in ARC's Nanofabrication Laboratory result in circular, square and hexagonal shapes. Considering the electric field is strongest in the vicinity of sharp edges, other shapes should be investigated. One idea for a shape of interest is shown in Figure 45.

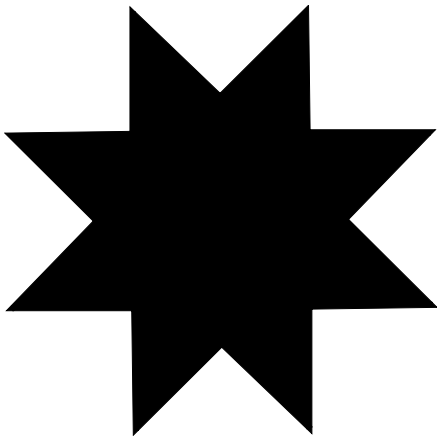

Figure 45. Eight-pointed Star Pillar.

Once the etching process is perfected, etching holes of shapes that may further contribute to the field enhancement factor, such as the one shown in Figure 46, should be investigated.

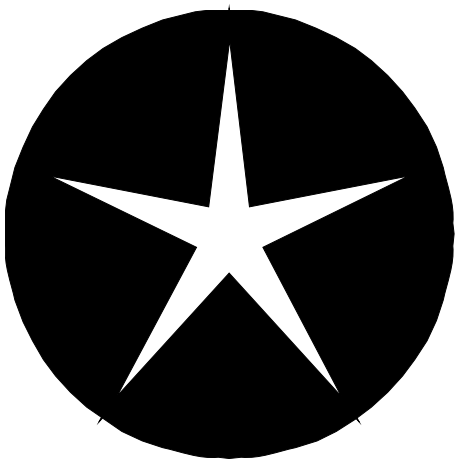

Figure 46. Five-pointed Hole in Circular Pillar.

The second geometric variable is pillar arrangement. Current masks available have the squares arranged in rows and columns, while the circles and hexagons are in staggered rows. Arrangements of both types in various pillar shapes should be explored. It is possible, however, that once the etching process is perfected, the pillar arrangement will be unimportant, since very little of the propellant will be flowing between pillars. Other array design elements that can be manipulated include pillar size and pillar pitch (the distance between the centers of adjacent pillars). Similar to pillar arrangement, these elements may have less effect on the performance of a flow-through electrode.

4. Detailed Testing and Characterization

Future tests should incorporate more detailed procedures for testing and characterizing electrodes. For instance, it is desirable to investigate the mechanisms of electrode erosion such as ionic breakdown and microarcing. Investigating these thoroughly will require the removal of the sample from the

FE/IC between each set of test runs for a given set of parameters, for characterization using the SEM. This will allow erosion to be more closely monitored and the effects on the electrode to be more closely associated with test parameters such as electrode gap spacing, argon pressure and applied fields. This will be a tedious and extremely time-consuming process, but only then will the conditions which best preserve the integrity of the electrode be identified, which will allow optimization of the operating environment.

5. Gate Electrode Fabrication and Integration

The next step in the development of a miniature ionizer section will have to be the fabrication and integration of a gate, or extractor, electrode. The gate electrode is essential to the proper functioning of the ionizer, as well as to its life expectancy. The ions being created at the tips of the CNTs must be extracted from the ionization region for two main reasons. First, if ions are allowed to build up in this region, microarcing may occur. Second, as previously shown, the ions are destructive to the CPA if not evacuated. Also, the gate electrode can act to focus the ions, greatly reducing their damaging impacts on the accelerator grid, thus increasing the life-expectancy of the thruster. Previous research at ARC has shown that a gate electrode may be constructed by many of the same processes used in the fabrication of the CPA electrode. This research must be extended to investigate the optimization of an integrated gate electrode for a flow-through ionizer.

6. Ionizer / Accelerator Integration

The final step in this work will be to integrate a complete, gated CPA electrode with a gridded accelerator electrode to make a complete miniature ion thruster. Other components will of course have to be sourced or fabricated, such as a miniature power-conditioning unit to generate the requisite voltage and power needed from the 12 or 24 volt supply of the spacecraft bus. Once a

propellant gas is selected, there will have to be an investigation into miniature tanks, feed systems and throttling valves, probably using microelectro-mechanical systems (MEMS).

THIS PAGE INTENTIONALLY LEFT BLANK

APPENDIX A. PROCEDURES

A. ION BEAM SPUTTERER OPERATION

1. Prior to initial sputtering, the silicon substrate must be thoroughly cleaned and dried.
    i. Clean substrate with acetone, followed by a rinse of deionized water. Repeat this step, ensuring sample is well-rinsed.
    ii. Dry sample by first removing visible water using compressed air, argon or nitrogen.
    iii. Place sample on a hot plate at 150ºC for 10-20 seconds, then set on a safe surface to cool. This step ensures the sample is completely dry.
2. Check Ion Beam Sputterer (IBS) logbook to ensure sputtering is not already in progress.
3. Check argon regulator pressure gauge to ensure sufficient argon pressure for IBS operation.
4. Attach samples to IBS stage using carbon tape. Ensure pieces are securely affixed to the stage prior to loading into the IBS.
5. Turn off pumps and allow pressure to bleed off until door is able to be opened; an audible hiss will be heard as the argon purges from the ion guns. Figure A-1 shows the interior of the IBS chamber with major components labeled.

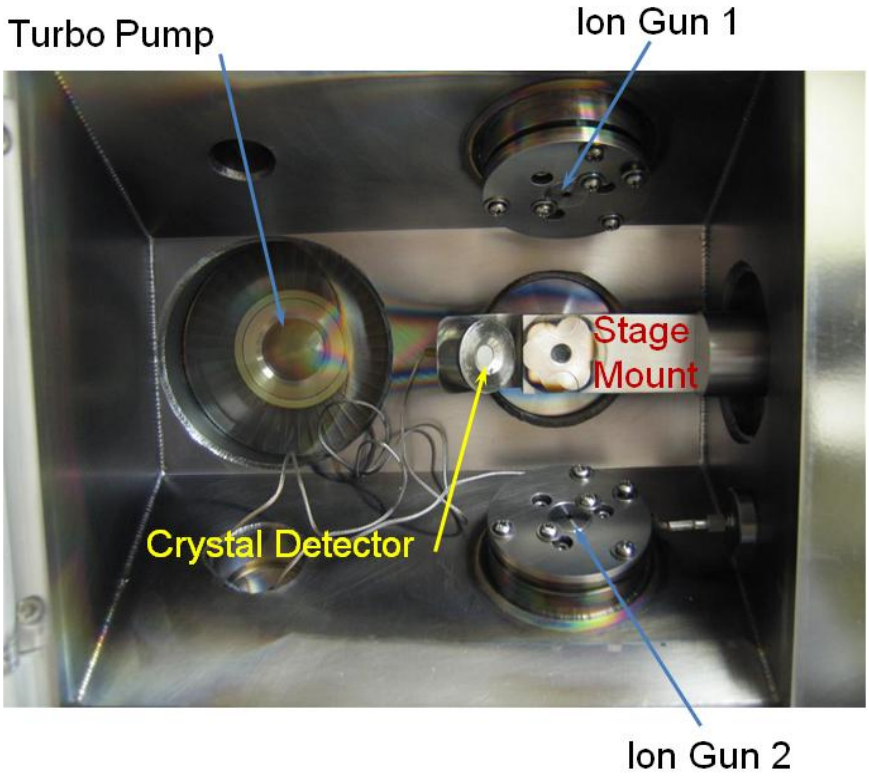

Figure A-1. IBS Chamber with Components Labeled.

6. Load targets and stage into the IBS. Use caution so as not to strip the set-screws holding the targets. Take note of which target is in which position prior to closing the door. Figure A-2 shows the rotary target mount inside the door of the IBS chamber.

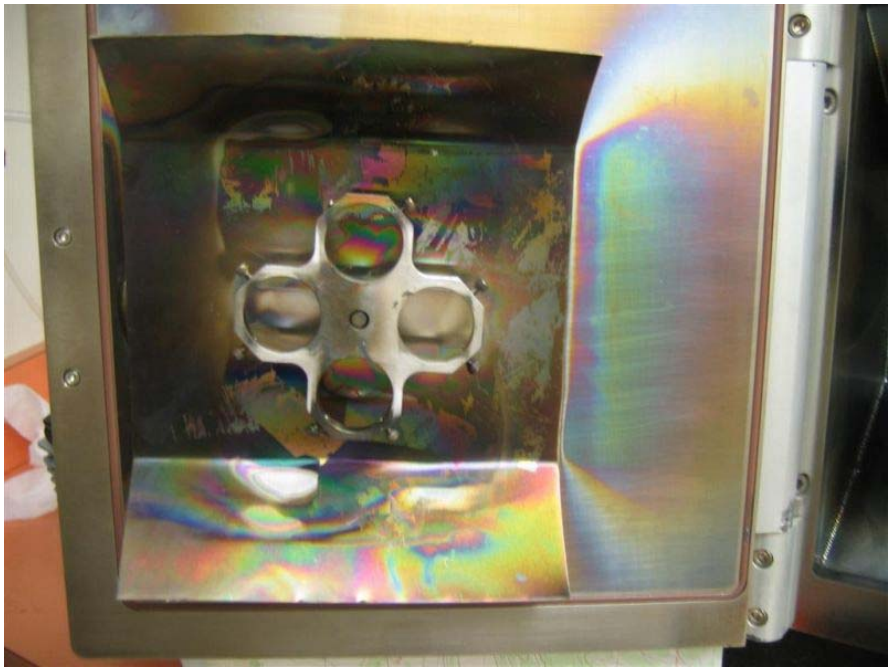

Figure A-2. IBS Target Mount / Selector.

7. Close door and start pumps. Whenever pumps are started, ensure that door is sealed by tugging lightly on the handle after approximately 5 seconds of pump operation.
8. Allow IBS to pump down for a minimum of 10 minutes to ensure adequate vacuum is achieved prior to commencing sputtering.
9. While IBS is pumping down, prepare the first round of sputtering.
    i. Log sputtering data and start time into IBS log.
    ii. Set rotary target selector to first target.
    iii. Set program information into the control panel (Figure A-3).
        1. Press ‘Program’ button to view the program settings and ‘Enter’ to cycle through them. Set values using up and down arrow buttons.
        2. Set preset target number. Preset targets include chromium, iron and molybdenum. Double-check the

values for density and Z-factor with the material properties chart on the wall to the left of the IBS.

3. Select preset nine (9) for user-defined targets. These include titanium, tantalum and platinum. Set density and Z-factor according to the material properties chart.

4. Once material properties have been checked or set, set ‘sputter’ and ‘end’ thickness values. These should always be set to the same value, as the sensor will be zeroed between each round of sputtering. Thicknesses values are in kiloangstroms (kÅ). 0.1 kÅ = 10 nm.

5. Once all settings are checked or set, as appropriate, press ‘Program’ button again to enter the program into the controller.

Figure A-3. IBS Programming Panel.

10. After the pump-down period, commence sputtering by pressing the ‘HV On/Off’ button (High Voltage) (see Figure A-4).

11. Allow amperage and voltage read-outs to settle (~30 seconds) then check that they are steady at 4.00 mA and 8.00 kV (see Figure A-4). If they are not, ask for assistance in setting these values.

Figure A-4. IBS Control Panel.

12. After the programmed end thickness has been achieved, the IBS will automatically shut off the ion guns, as indicated by the HV On/Off lamp going out.
13. Turn off pumps. Retrieve targets, stage and samples.
14. Close door and turn pumps back on to maintain IBS chamber under vacuum. This keeps the chamber clean and free of moisture.
15. Log sputtering end time in the IBS logbook.

B. ETCHING

1. *All etching must be performed under the fume hood.*
2. Place a wide, low glass dish on the feedback-controlled hot plate. Near its center, place a small beaker of 50% potassium hydroxide (KOH). *Use extreme caution when handling KOH*. Ensure the beaker is at least half full, otherwise it will be unstable in the water bath. Cover the KOH with a beaker cover to minimize fumes and evaporative losses.
3. Fill the wide, low dish with deionized water as full as possible without disturbing the stability of the KOH beaker. The more water in the bath, the less frequent it will require refilling. Place the temperature control probe into the water near, but not touching, the beaker of KOH. Ensure the probe is not resting on the bottom of the dish; approximately half depth is the desired placement (see Figure A-5 (a) and (b)).

(a)  (b) 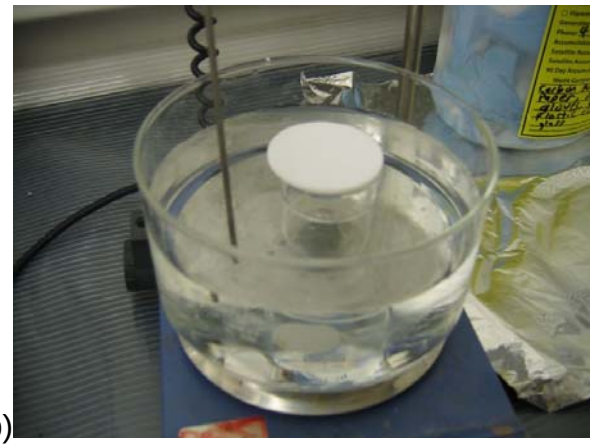

Figure A-5. (a) KOH Etching Setup. (b) Close-up of Water Bath and KOH Beaker

4. Set temperature controls to maintain 80ºC. Etch rate is highly temperature dependent. It is therefore very important to maintain the process as near to 80ºC as possible so that the etch rate will be consistent.

5. Set a beaker of deionized water on a nearby hotplate also set to 80ºC. This will be used to replenish water evaporated from the water bath without adversely altering the bath's temperature.

6. When the water bath has reached steady-state at the programmed temperature, remove the beaker cover and place on metal foil. *Using plastic tweezers*, place the sample into the KOH; replace beaker cover. *Always rest any items contaminated with KOH (beaker cover, tweezers, etc.) on metal foil beneath the fume hood.*

7. Approximately once per hour, replenish water lost from the water bath. Check the level of KOH as well, but with the beaker cover in place, KOH evaporation is minimal.

8. After desired etch depth is achieved, remove sample and rinse extremely well using deionized water. Dry with compressed air, nitrogen or argon.

9. Clean up etching equipment, ensuring all liquids are disposed of in the appropriate HAZMAT container and all containers are rinsed thoroughly before being returned to the drying rack.

C. PHOTOLITHOGRAPHY

1. Turn on power supply for the high-intensity ultraviolet (UV) lamp. The power supply requires a warm-up period, so do not start the UV lamp at this time (see Figure A-6).

Figure A-6. High-power UV Lamp Power Supply.

2. Spin-coat sample with photoresist.

    i. Check spin-coater program. Use ‘Program Select’ to choose program; check program parameters using ‘F1’ and ‘Step’ keys. Program should be 500 RPM for 15 seconds followed by 2000 RPM for two minutes (see Figure A-7).

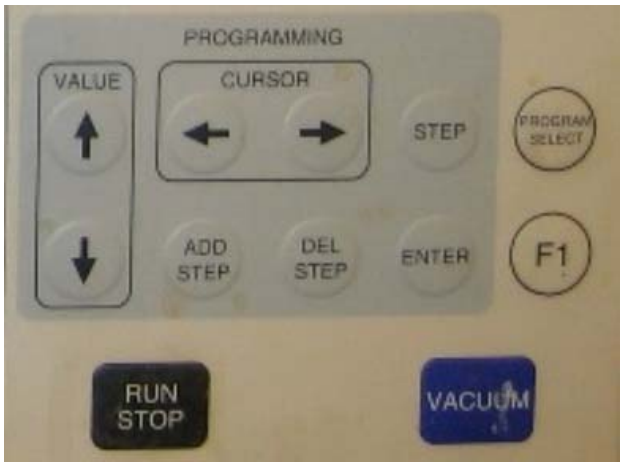

Figure A-7. Spin-coater Control Panel.

ii. Place sample onto vacuum chuck and press ‘Vacuum’ button. Ensure vacuum reading on display is at least 18 (see Figure A-8).

Figure A-8. Spin-coater.

iii. After closing lid, prepare a half-full dropper of photoresist to apply to sample.

iv. Press start and observe the speed settle at 500 RPM. Apply photoresist through hole in lid. *All photoresist must be applied during the 15-second first phase of the program.*

v. Machine will automatically stop after program is complete.

3. Check spin-coat is even and defect free in the area to be patterned. If the center of the sample is defective, clean the piece with acetone, rinse with deionized water, dry well and reapply the spin-coat.

4. In order for the photoresist to become photosensitive, it must be soft-baked. Soft-bake the photoresist by placing sample on a

hotplate set to 130ºC. After 30 seconds, remove sample and set on a glass slide or other cool surface for 1-2 minutes.

5. Place sample on the table of the mask alignment machine. Using the attached microscope, ensure the desired mask is near the center of the sample. Also, check that the mask is lying flat and evenly contacting the surface to be patterned. *Insufficient mask contact will result in a low resolution pattern*.
6. Start the UV lamp.
7. Check that lamp exposure timer is turned on and set for a five (5) second exposure. Slide table under lamp; exposure will occur automatically for the period set into the timer. *Look away from the machine while exposure is occurring. Ensure other samples are covered to prevent their exposure to the UV lamp.* Slide table back and remove sample.
8. Place sample on a hotplate set to 140ºC. After one (1) minute, remove sample and set on a glass slide or other cool surface for 1-2 minutes.
9. Develop the photoresist by placing a surface-tension bubble of developer on the sample for 30 seconds. Rinse the sample well, ensuring all of the developer is rinsed away; otherwise, the photoresist may be overdeveloped.
10. Dry the sample thoroughly using compressed air. Inspect the pattern for proper development. All unpatterned areas of the sample should be shiny and free of photoresist. If not, the piece is underdeveloped. If underdevelopment is apparent, develop again for 15 seconds.

11. Clean all unpatterned areas using acetone. *Take extreme care not to destroy the pattern.* Rinse well with deionized water, then dry using compressed air.

12. Inspect the pattern using the optical microscope. If the pattern is damaged or otherwise unsuitable, clean the sample with acetone, rinse with deionized water, dry well and repeat the lithography procedure. The pattern should look like the one shown in Figure A-9. The resolution of the pattern is best seen using the periphery lighting filter on the optical microscope (see Figure A-10). This will show how sharply the pattern was transferred during the photolithographic process, but will not give any indication of its suitability for lift-off, as does the aforementioned view shown in Figure A-9.

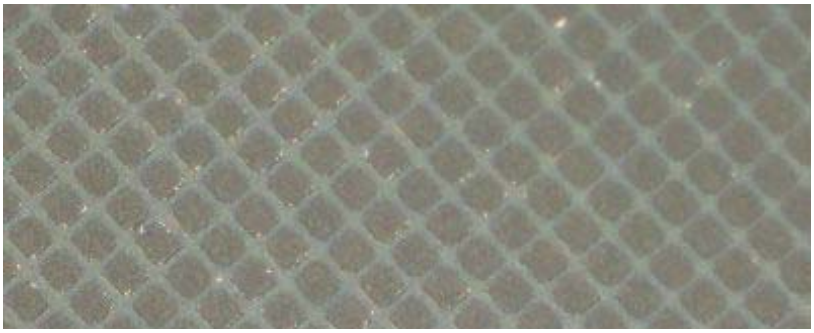

Figure A-9. Patterned Photoresist at 5x Magnification.

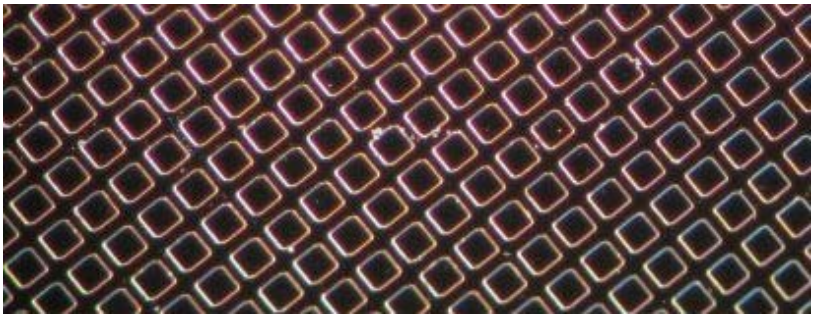

Figure A-10. Patterned Photoresist at 5x Magnification (Periphery Lighting).

D. THERMAL CHEMICAL VAPOR DEPOSITION

1. Bake out growth tube to remove any impurities (as required).
    i. Place tube in furnace with no fittings attached and the inlet end flush with the side of the furnace. Check that the exhaust end of the tube is in the vacuum exhaust. Close furnace and set temperature to desired growth temperature.
    ii. After 30 minutes, slide tube in furnace so that the exhaust end is now flush with the side of the furnace. Move furnace to place it as close as practicable to the vacuum exhaust.
    iii. After 30 minutes, open furnace and allow tube to cool below 200ºC.
2. When tube is cool enough to handle, attach exhaust fitting to the appropriate end of the growth tube. Before attaching fittings, inspect o-rings for cracks or splits.
3. Place sample(s) into growth tube. If only one sample is being grown on, position it such that it is slightly downstream of the thermocouple. If more than one sample is being used, ensure that the most upstream sample is even with the thermocouple as shown in Figure A-11. The temperature in the furnace is much more consistent downstream of the thermocouple compared to upstream. Therefore, growth will be more consistent with the samples arranged as shown.

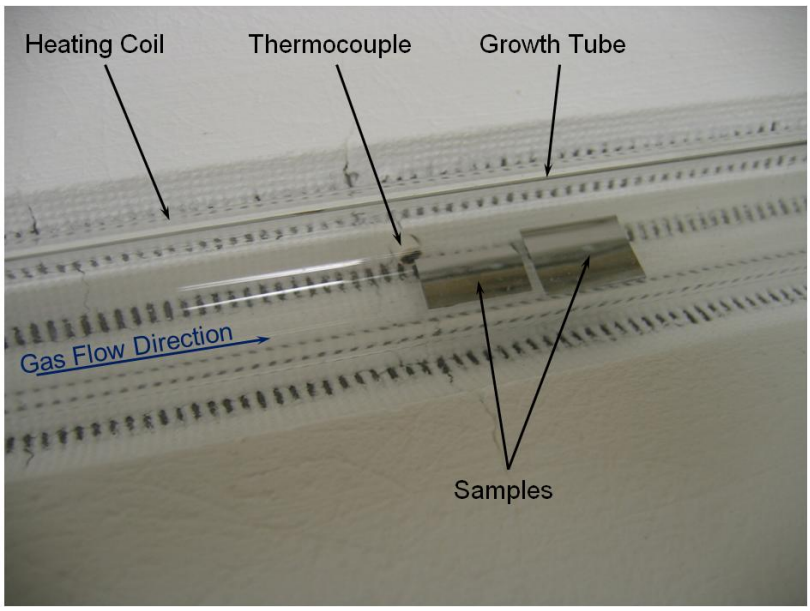

Figure A-11. Correct Sample Placement With Respect to Thermocouple.

4. Attach gas supply fitting to inlet end of the growth tube (see Figure A-12).

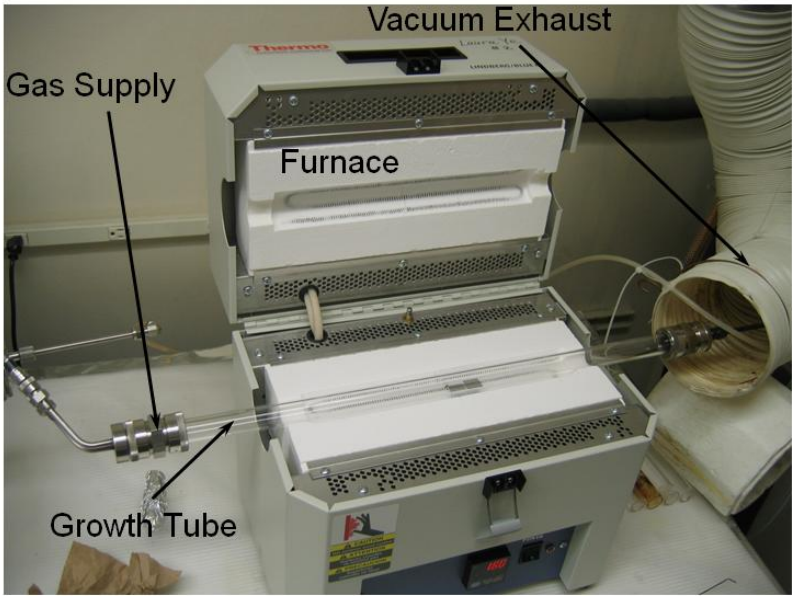

Figure A-12. TCVD Tube Furnace.

5. Open all tank valves and regulators for gas supplies. Ensure feed pressure is at least 20 psi for all tanks.

6. Turn on mass-flow controller (MFC). Turn channels 1 and 2 on; 3 and 4 should be off (see Figure A-13).

Figure A-13. Mass-flow Controller.

7. Turn supply valves for channels 1 and 2 to argon. Check that mass-flow rates for both channels are set to the desired levels (see Figure A-13 and Figure A-14).

Figure A-14. Gas Flow Control Panel.

8. Close furnace and check it is set to the desired growth temperature (see Figure A-15).

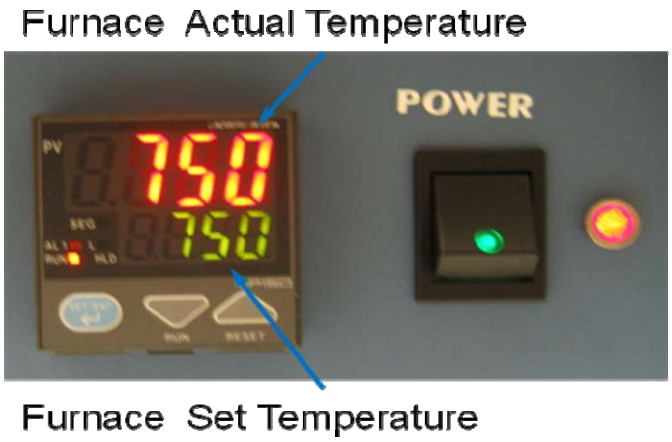

Figure A-15. TCVD Furnace Control Panel.

9. Once the furnace has reached the set temperature, continue flowing 100% argon for 10 minutes.
10. Switch channel 1 to hydrogen. Flow this gas mixture for 5 minutes.
11. Switch channel 2 to ethylene. Flow this gas mixture for 30 seconds to 10 minutes, depending on desired CPA height.
12. Switch channels 1 and 2 to argon. Flow 100% argon for 5 minutes.
13. Open furnace. Continue flowing 100% argon until furnace has cooled below 200ºC.
14. Secure channels 1 and 2; close tank valves and regulators; turn MFC off.
15. Remove inlet and exhaust fittings. Place tube in cooling rack to remove samples.
16. Repeat bake-out procedure before storing tube. Store tube with ends sealed to prevent contamination.

E. FIELD EMISSION / IONIZATION CHAMBER SETUP

1. Secure the turbo pump.
2. When chamber pressure has reached approximately $5x10^{-1}$ Torr, secure the roughing pump. This bleed-down will take approximately 30 minutes. *If the roughing pump is secured too soon, the turbo pump will be insufficiently backed and may be permanently damaged*.
3. Open the small relief valve on the bottom of the turbo pump, allowing the chamber to equalize to atmospheric pressure, $7.5x10^{2}$ Torr. Once equalized, close the relief valve.
4. Remove the upper stage of the FE/IC by extracting the six retaining bolts using the correct triple-square wrench. *Refer to Figure 28 for the location of described components*.
5. Lay upper stage securely on a flat work surface
6. Remove lower electrode stage (LES) by extracting the small Allen screws. *Use caution not to strip the threads in the plastic collar*.
7. Mount sample to stage using carbon tape. Ensure the CPA, not the entire electrode, is centered on the stage. Leave the sample somewhat loose so that it may be manipulated once the LES is reinstalled.
8. Check configuration of upper electrode. There are two types of upper electrodes, one with a plastic mount and one with a metal mount. Using the metal mount will ground the electrode to the apparatus, preventing the configuration of the device as an anode. Ensure the upper electrode is of the correct configuration for all planned experiments.
9. Reinstall LES. Mounting screws should be hand-tightened to prevent stripping the threads in the plastic mounting collar.

10. Center CPA precisely below the upper electrode using tweezers. This will ensure maximum performance and minimize likelihood of electrode burnout.

11. Clamp sample with the lower lead, known as the ‘paperclip’, using tweezers. Ensure paperclip will remain clear of the upper electrode throughout the micrometer’s range of adjustment. *Use caution not to contact the lower electrode with the upper one during this check*. The correct arrangement of components at this stage is shown in Figure A-16.

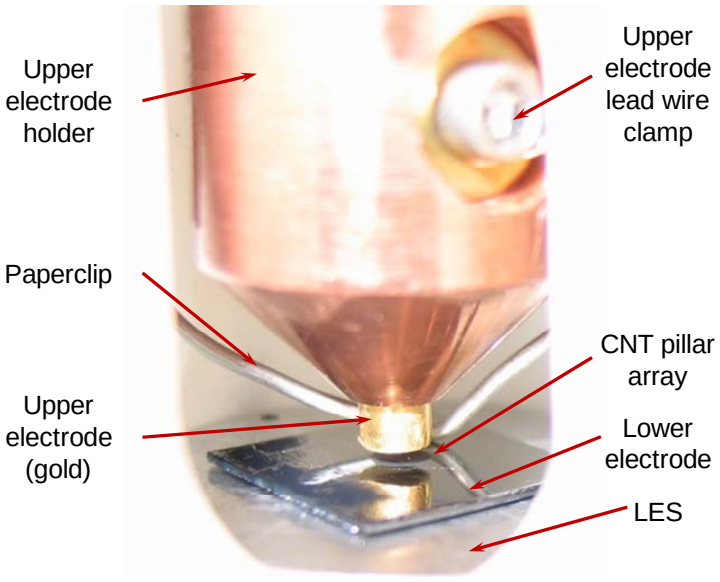

Figure A-16. Detailed View of Components in FE/IC Upper Stage.

12. Retract upper electrode using micrometer to allow a safety gap between electrodes for upper stage reinstallation.

13. Check continuity of the upper electrode and paperclip to their respective leads using a multimeter.

14. Measure the resistance between the surface of the lower electrode and its respective lead. This value should be less than 200Ω.

15. Place ‘anode’ and ‘cathode’ labels on the correct leads.

16. Reinstall upper stage using a new copper crush seal. Tighten retaining bolts in a ‘lug’ pattern to maintain even contact all the way around the flange and copper crush seal. *Do not over-tighten the retaining bolts*.
17. Check Keithley 237 output is at the desired voltage using a multimeter.
18. Connect Keithley 237 output to FE/IC leads in the desired configuration.
19. Start the roughing pump.
20. When FE/IC pressure reaches $5x10^{-1}$ Torr, start the turbo pump. Achieving 10^{-5} Torr will take approximately 10 minutes. Higher vacuum levels will take exponentially longer times. 10^{-8} Torr requires approximately 12 hours.

APPENDIX B. DATA TABLES

A. ELECTRODE 1

1. Ultrahigh Vacuum

Gap (μm)	Turn-On Voltage (V)	Applied Field (V/μm)
10	115	11.50
20	153	7.65
30	181	6.03
40	216	5.40
50	237	4.74
60	N/A	N/A
70	N/A	N/A

Table 7. Turn-on Voltages and Applied Field Strengths for Various Electrode Gaps (Electrode 1, UHV).

Gap (μm)	Compliance Voltage (V)	Applied Field (V/μm)
10	137	13.70
20	178	8.90
30	216	7.20
40	N/A	N/A
50	N/A	N/A
60	N/A	N/A
70	N/A	N/A

Table 8. Compliance Voltages and Applied Field Strengths for Various Electrode Gaps (Electrode 1, UHV).

2. Static Low-pressure Argon

Electrode 1 was not tested in an argon environment.

B. ELECTRODE 2

1. Ultrahigh Vacuum

Gap (μm)	Turn-On Voltage (V)	Applied Field (V/μm)
10	229	22.90
20	299	14.95
30	370	12.33
40	450	11.25
50	522	10.44
60	592	9.87

Table 9. Turn-on Voltages and Applied Field Strengths for Various Electrode Gaps (Electrode 2, UHV).

Gap (μm)	Compliance Voltage (V)	Applied Field (V/μm)
10	357	35.70
20	479	23.95
30	605	20.17
40	727	18.18
50	843	16.86
60	965	16.08

Table 10. Compliance Voltages and Applied Field Strengths for Various Electrode Gaps (Electrode 2, UHV).

2. Static Low-pressure Argon

Argon Pressure (Torr)	Turn-On Voltage (V)	Applied Field (V/μm)
2.40E-06	232	23.20
2.40E-05	194	19.40
2.40E-04	159	15.90
2.40E-03	146	14.60
2.40E-02	76	7.60

Table 11. Field Emission Turn-on Voltages and Applied Field Strengths for Various Argon Pressures (Electrode 2, 10μm Gap).

Argon Pressure (Torr)	Compliance Voltage (V)	Applied Field (V/μm)
2.40E-06	355	35.50
2.40E-05	331	33.10
2.40E-04	264	26.40
2.40E-03	255	25.50
2.40E-02	232	23.20

Table 12. Field Emission Compliance Voltages and Applied Field Strengths for Various Argon Pressures (Electrode 2, 10μm Gap).

C. ELECTRODE 3

1. Ultrahigh Vacuum

Gap (μm)	Turn-On Voltage (V)	Applied Field (V/μm)
10	107	10.70
20	157	7.85
30	199	6.63
40	242	6.05
50	283	5.66
60	327	5.45
70	372	5.31

Table 13. Turn-on Voltages and Applied Field Strengths for Various Electrode Gaps (Electrode 3, UHV).

Gap (μm)	Compliance Voltage (V)	Applied Field (V/μm)
10	172	17.20
20	253	12.65
30	338	11.27
40	388	9.70
50	461	9.22
60	538	8.97
70	618	8.83

Table 14. Compliance Voltages and Applied Field Strengths for Various Electrode Gaps (Electrode 3, UHV).

2. Static Low-pressure Argon

Argon Pressure (Torr)	Turn-On Voltage (V)	Applied Field (V/μm)
2.20E-06	344	6.88
2.20E-05	430	8.60
2.20E-04	368	7.36

Table 15. Field Ionization Turn-on Voltages and Applied Field Strengths for Various Argon Pressures (Electrode 3, 50μm Gap).

Argon Pressure (Torr)	Turn-On Voltage (V)	Applied Field (V/μm)
2.20E-06	554	11.08
2.20E-05	N/A	N/A
2.20E-04	N/A	N/A

Table 16. Field Ionization Compliance Voltages and Applied Field Strengths for Various Argon Pressures (Electrode 3, 50μm Gap).

Argon Pressure (Torr)	Turn-On Voltage (V)	Applied Field (V/μm)
2.20E-06	382	7.64
2.20E-05	354	7.08
2.20E-04	358	7.16

Table 17. Field Emission Turn-on Voltages and Applied Field Strengths for Various Argon Pressures (Electrode 3, 50μm Gap).

Argon Pressure (Torr)	Turn-On Voltage (V)	Applied Field (V/μm)
2.20E-06	632	12.64
2.20E-05	194	3.88
2.20E-04	76	1.52

Table 18. Field Emission Compliance Voltages and Applied Field Strengths for Various Argon Pressures (Electrode 3, 50μm Gap).

D. ELECTRODE 4

1. Ultrahigh Vacuum

Gap (μm)	Turn-On Voltage (V)	Applied Field (V/μm)
10	116	11.60
20	150	7.50
30	176	5.87
40	198	4.95
50	231	4.62
60	270	4.50
70	289	4.13

Table 19. Turn-on Voltages and Applied Field Strengths for Various Electrode Gaps (Electrode 4, UHV).

Gap (μm)	Compliance Voltage (V)	Applied Field (V/μm)
10	189	18.90
20	248	12.40
30	291	9.70
40	328	8.20
50	394	7.88
60	444	7.40
70	484	6.91

Table 20. Compliance Voltages and Applied Field Strengths for Various Electrode Gaps (Electrode 4, UHV).

2. Static Low-pressure Argon

Argon Pressure (Torr)	Turn-On Voltage (V)	Applied Field (V/μm)
2.20E-06	263	5.26
2.20E-05	468	9.36
2.20E-04	582	11.64

Table 21. Field Ionization Turn-on Voltages and Applied Field Strengths for Various Argon Pressures (Electrode 4, 50μm Gap).

Argon Pressure (Torr)	Turn-On Voltage (V)	Applied Field (V/μm)
2.20E-06	692	13.84
2.20E-05	908	18.16
2.20E-04	1012	20.24

Table 22. Field Ionization Compliance Voltages and Applied Field Strengths for Various Argon Pressures (Electrode 4, 50μm Gap).

Argon Pressure (Torr)	Turn-On Voltage (V)	Applied Field (V/μm)
2.20E-06	224	4.48
2.20E-05	242	4.84
2.20E-04	247	4.94

Table 23. Field Emission Turn-on Voltages and Applied Field Strengths for Various Argon Pressures (Electrode 4, 50μm Gap).

Argon Pressure (Torr)	Turn-On Voltage (V)	Applied Field (V/μm)
2.20E-06	378	7.56
2.20E-05	412	8.24
2.20E-04	396	7.92

Table 24. Field Emission Compliance Voltages and Applied Field Strengths for Various Argon Pressures (Electrode 4, 50μm Gap).

APPENDIX C. MATLAB CODES

A. CODE FOR DATA EXTRACTION FROM EXCEL FILES

```
%   Vacuum: Various, as noted
%   Argon = Yes
%   22 NOV 08
%   Electrode 2

clc, clear all, close all

%%  Argon Pressure 2.4E-6 Torr

[x1,TXT,RAW] = XLSREAD('22NOV_Argon.xlsx','2.4E-6','g3:g357');
[y1,TXT,RAW] = XLSREAD('22NOV_Argon.xlsx','2.4E-6','h3:h357');
y1 = y1/1e-3;

%%  Argon Pressure 2.4E-5 Torr

[x2,TXT,RAW] = XLSREAD('22NOV_Argon.xlsx','2.4E-5','g3:g329');
[y2,TXT,RAW] = XLSREAD('22NOV_Argon.xlsx','2.4E-5','h3:h329');
y2 = y2/1e-3;

%%  Argon Pressure 2.4E-4 Torr

[x3,TXT,RAW] = XLSREAD('22NOV_Argon.xlsx','2.4E-4','g3:g272');
[y3,TXT,RAW] = XLSREAD('22NOV_Argon.xlsx','2.4E-4','h3:h272');
y3 = y3/1e-3;

%%  Argon Pressure 2.4E-3 Torr

[x4,TXT,RAW] = XLSREAD('22NOV_Argon.xlsx','2.4E-3','g3:g258');
[y4,TXT,RAW] = XLSREAD('22NOV_Argon.xlsx','2.4E-3','h3:h258');
y4 = y4/1e-3;

%%  Argon Pressure 2.4E-2 Torr

[x5,TXT,RAW] = XLSREAD('22NOV_Argon.xlsx','2.4E-2','g3:g235');
[y5,TXT,RAW] = XLSREAD('22NOV_Argon.xlsx','2.4E-2','h3:h235');
y5 = y5/1e-3;


%%  Summary Plot
```

```
figure (20),
plot (x1, y1, 'kv', x2, y2, '^', x3, y3, 'o', x4, y4, 'x',...
   x5, y5, 'd', 'markersize', 5);

grid on
xlabel ('Voltage (V)')
ylabel ('Current (mA)')
legend ('2.4E-6', '2.4E-5', '2.4E-4', '2.4E-3', '2.4E-2', 2);

figure (21),
semilogy (x1, y1*1e-3, 'kv', x2, y2*1e-3, '^', x3, y3*1e-3, 'o', ...
         x4, y4*1e-3, 'x', x5, y5*1e-3, 'd', 'markersize', 5);

ylim ([1e-9 1e-4]);
xlabel ('Voltage (V)')
ylabel ('Current (A)')
legend ('2.4E-6', '2.4E-5', '2.4E-4', '2.4E-3', '2.4E-2', 4);
```

B. CODE FOR PLOTTING FOWLER-NORDHEIM FITS

```
%   Vacuum: 2.7E-7 Torr
%   Argon = No
%   6 DEC 08
%   Electrode 4
%   50 Micron Gap

clc, clear all, close all

[x5,TXT,RAW] = XLSREAD('6DEC_UHV.xlsx','50micron','g3:g396');
[y5,TXT,RAW] = XLSREAD('6DEC_UHV.xlsx','50micron','h3:h396');
y5 = y5/1e-3;

x55 = 1./x5;
y55 = log(y5./(x5.^2));
p5 = polyfit(x55(232:end),y55(232:end), 1);
y555 = p5(1).*x55 + p5(2);
beta = -6.831e9*5^1.5/p5(1)
gamma = beta * 50e-6

figure (55),
plot (x55(232:end),y55(232:end), 'o', ...
   x55(232:end),y555(232:end), 'r', 'markersize', 5, 'linewidth', 2);
grid on
xlabel ('1/V')
```

```
ylabel ('ln( I / V^{ 2})')
legend ('This Work', 'F-N Model')
```

THIS PAGE INTENTIONALLY LEFT BLANK

LIST OF REFERENCES

[1] M. Wright, “Ion Propulsion: Over 50 Years in the Making,” [http://science.nasa.gov/newhome/headlines/prop06apr99_2.htm]. September 2008.

[2] Wikipedia, “Ion Thruster” [http://en.wikipedia.org/wiki/Ion_thruster]. September 2008.

[3] G. R. Brewer, *Ion Propulsion Technology and Applications*, Gordon and Breach Science Publishers, NY, 1970.

[4] E. Stuhlinger, *Ion Propulsion for Space Flight*, McGraw-Hill, New York, 1964.

[5] G. B. Ganapathi, “Performance of the Xenon Feed System on Deep Space One,” Journal of Spacecraft and Rockets, AIAA, Vol. 37, No. 3, May 2000.

[6] Wikipedia, “Deep Space 1” [http://en.wikipedia.org/wiki/Deep_Space_1]. November 2008.

[7] M. Rayman, “Dawn, A Journey to the Beginning of the Solar System” [http://www-ssc.igpp.ucla.edu/dawn/mission.html]. November 2008.

[8] R. G. Jahn, *Physics of Electric Propulsion*, Dover Publications Inc., Mineola, 1968.

[9] G. P. Sutton and O. Biblarz, *Rocket Propulsion Elements*, 7th Edition, Wiley, NY, 2001.

[10] O. Biblarz and J. Sinibaldi, “Study of DC Ion Thrusters with Argon Propellants,” JPC paper AIAA 2006-4670, Sacramento, CA, 2006.

[11] R. Gomer, *Field Emission and Field Ionization*, American Institute of Physics, New York, 1962.

[12] H. Fanghor, “Mechanical, acoustic and thermal properties of nanostructures” [http://www.soton.ac.uk/~fangohr/ research/cnt.html]. September 2008.

[13] University of Surrey, “UniS Materials Institute” [http://www.umi.surrey.ac.uk/people/profiles/postgrads?s_id=315]. September 2008.

[14] Wikipedia, “Carbon Nanotube” [http://en.wikipedia.org/wiki/Carbon_nanotube]. September 2008.

[15] J. L. Killian et al, “Field emission properties of carbon nanotube pillar arrays,” Journal of Applied Physics, American Institute of Physics, Vol. 103, No. 6, March 2008.

[16] J. P. Singh et al, “Field ionization of argon using β-phase W nanorods,” Applied Physics Letters, American Institute of Physics, Vol. 85, No. 15, October 2004.

[17] N. Koratkar, “Nanoscale field ionization sensors: A review,” International Journal of Nanoscience, World Scientific, Vol. 4, Nos. 5 & 6, 2005.

[18] L. F. Velasquez and A. I. Akinwande, “A PECVD CNT-based open architecture field ionizer for portable mass spectrometry,” MEMS, 2008.

[19] D. L. Niemann, “Experimental and Theoretical Investigations of Field Emission in Carbon Nanotubes and their Multiscale Integrated Systems,” Doctoral Thesis, Santa Clara University, Santa Clara, CA, June 2008.

INITIAL DISTRIBUTION LIST

1. Defense Technical Information Center
   Ft. Belvoir, VA

2. Dudley Knox Library
   Naval Postgraduate School
   Monterey, CA

3. Head, Information Operations and Space Integration
   Branch, PLI/PP&O/HQMC
   Washington, DC

4. Professor Oscar Biblarz
   Department of Mechanical and Astronautical Engineering
   Naval Postgraduate School
   Monterey, CA

5. Professor Marcello Romano
   Department of Mechanical and Astronautical Engineering
   Naval Postgraduate School
   Monterey, CA

6. Dr. Minoru Freund
   NASA Ames Research Center
   Moffett Field, CA

7. Dr. Cattien V. Nguyen
   NASA Ames Research Center
   Moffett Field, CA

8. Dr. Darrell L. Niemann
   NASA Ames Research Center
   Moffett Field, CA